Title

Ultrathin electron and proton-conducting membranes for nanoscale integrated artificial photosystems

Journal

Sustainable Energy & Fuels, 7(14)

ISSN

2398-4902

Author

Frei, Heinz

Publication Date

2023-07-11

DOI

10.1039/d3se00499f

Ultrathin electron and proton conducting membranes for nanoscale integrated artificial photosystems

Heinz Frei

Molecular Biophysics and Integrated Bioimaging Division, Lawrence Berkeley National Laboratory, University of California, Berkeley, CA 94720

e-mail: HMFrei@lbl.gov

(*Sustain. Energy Fuels* **7**, 3213-3231 (2023): DOI: 10.1039/d3se00499f)

Abstract

Reducing the thickness of separation membranes without compromising selectivity and robustness is the most effective way of maximizing areal conductivity. This is especially important for the integration of visible light driven water oxidation and carbon dioxide (or proton) reduction into a complete artificial photosystems on the shortest possible length scale – the nanoscale – because of the efficiency advantages over macroscale photosystems. In addition to excellent separation property, ultrathin membranes of ten nanometer thickness or less need to exhibit sufficient electrical and proton conductivity in order for the photocatalytic rates to keep up with the photon flux at maximum solar intensity. Two materials, graphene and amorphous silica with embedded molecular wires, have emerged as promising ultrathin membranes for the development of nanoscale integrated solar fuel systems. Moreover, electrically conducting metal-organic or covalent organic frameworks offer high surface area supports that enable the use of molecular catalysts and/or light absorbers at adequate areal density for nanoscale integration with graphene membranes. Following an overview of the electron and proton conductivity of these ultrathin materials and recent examples of photoelectrocatalytic applications that take advantage of some but not all properties that constitute a complete functional membrane, the status and future opportunities for complete nanoscale integrated photosystems featuring an ultrathin membrane are discussed.

1. Introduction

The urgent need for energy dense liquid hydrocarbon fuels for sustainable transportation on a global scale that avoid fossil carbon sources, and for long term storage of renewable electricity is well established by now.[1] The generation of renewable fuels by artificial photosynthesis offers an attractive solution, to a significant extent because this approach for making fuels from sunlight, an inexhaustible source of energy, obviates the use of land needed for growing crop. Progress over the past decade in the development of efficient integrated systems for H_2 production by solar water splitting, and for the conversion of CO_2 and H_2O to CO or formate driven by sunlight with power efficiencies reaching 20 percent has been very impressive.[2-11] However, a major challenge for realizing an artificial photosynthesis technology is to reach a sufficient scale for impact on keeping fossil carbon in the ground on a global scale, which requires on the order of 10 terawatt of synthetic fuel from solar and wind in the coming decades.[1] While the most recently reported H_2O splitting and CO_2 reduction systems meet the essential requirement of exclusively using Earth abundant materials, it alone is not sufficient. Scalability at such an unprecedented level demands a minimal set of systems components and, in particular, avoidance of those that require replenishment or frequent replacement for sustained operation. Yet, these factors are not adequately addressed by existing artificial photosystems.

Natural photosynthesis, which makes sugar molecules from atmospheric CO_2 and H_2O using the energy of the sun, is the only existing system for making high energy chemicals on the terawatt scale (120 TW).[12] Therefore, the design principles that enable the scale of natural photosynthesis are worth considering. An important design aspect of the natural photosystem is that it closes the photosynthetic cycle of oxidizing H_2O and generating the primary reduction intermediate (Nicotinamide Adenine Dinucleotide Phosphate cofactor (NADPH)) on the

nanometer scale under membrane separation of the incompatible redox catalysis environments. A key feature is the less than 10 nm thick thylakoid separation membrane that affords electron transfer along embedded, hierarchically arranged molecular charge transfer components (chlorophyll, pheophytins, quinones, plastocyanines) and enables transport of protons by cyctochrome *bf* and ATPase enzymes (ATP = Adenosine triphosphate). At the same time, the thylakoid membrane blocks the products O_2 and NAPDH from crossover thereby preventing efficiency-degrading back and side reactions.[13] Such an ultrathin electron and proton conducting separation membrane may hold the key for enabling scalability of an artificial photosystem on the TW scale because it would allow minimizing the number of systems components and avoid ingredients prone to rapid degradation, especially by exploring designs exclusively involving gaseous reactants. Moreover, completing the photosynthetic cycle on the nanometer scale allows bypassing of major efficiency degrading processes intrinsic to the macroscale, in particular resistance losses caused by ion transport over micrometer and longer distances, and loss of charge by providing the shortest possible, molecularly defined transfer pathways.

Robust artificial membranes sufficiently thin for enabling nanoscale integration of artificial photosystems (< 10 nm) are far less developed than other essential systems components, i.e. light absorbers and catalysts. An important membrane criterion is direct, controlled electron transfer and proton transport at high enough rates for keeping up with the photon flux at maximum solar intensity while blocking small molecules like O_2 from crossover. The majority of existing separation membranes used in the field of artificial photosynthesis is based on organic polymers such as Nafion (perfluorosulfonic acid polytetrafluoroethylene copolymer) or Neosepta (polymer consisting of trimethylammonium substituents on arylalkane backbone) that are H^+ or OH^- conducting and gas separating, but not electrically conducting.[14,15] The ion conductivity of

these materials is based on fixed charged groups such as sulfonate or ammonium that promote transfer of H^+ (OH^-) ions while blocking mobile ions with the same charge. While suitable for membrane thicknesses of tens of μ, these cation- and anion-exchange membranes are not adequate for small molecule separation for thicknesses in the 10 nm range. The same holds for polymer membranes that are simultaneously electron conducting, such as poly(3,4-ethylenedioxythiophene)-poly(styrene sulfonate) (PEDOT:PSS).[14,16] Furthermore, ultrathin organic polymer membranes do not block crossover of energy dense hydrocarbon fuel products of deep CO_2 reduction.

Following a brief account of early explorations of ultrathin layers for spatial compartmentalization of photocatalytic components, this article focuses on recent progress in the development of ultrathin membranes that demonstrates the feasibility of thickness below 10 nm for preventing crossover of small molecules while exhibiting adequate charge and proton conductivity. Specifically, two types of materials have emerged, namely ultrathin amorphous silica layers and graphene sheets. Furthermore, for artificial photosystems featuring *molecular* catalysts, ultrathin 2D metal-organic or 2D covalent organic frameworks with adequate electron and proton conductivity may play a critical role in enabling the integration of such catalysts at sufficiently high areal density with ultrathin separation membranes. Transport properties of these materials and opportunities for building nanoscale integrated photosystems featuring ultrathin membranes, including approaches of their assembly into macroscale systems, will be discussed.

2. Early exploration of ultrathin layers for the spatial compartmentalization of photocatalytic components

Ultrathin layer-type materials in the form of 2D metal oxide nanosheets with light-induced charge transfer characteristics were identified in the early 1980s as opportunities for increasing photocatalytic efficiency by spatially organizing catalytic components. Following the demonstration of layered metal oxides as semiconductor photocatalysts for overall water splitting by Domen, Onishi and coworkers,[17,18] Mallouk exploited the occlusion of small, H_2-evolving (< 1 nm) Pt catalyst particles in interlayer spaces for blocking efficiency-degrading back charge transfer reactions.[19-21] Specifically, Pt loaded layered niobates like $K_4Nb_6O_{17}$ functionalized by adsorbed photosensitizer RuL_3 (L = 4,4'-dicarboxy-2,2'-bipyridine) afforded visible light driven generation of H_2 from HI by virtue of blocking the concurrently produced I_3^- upon I^- oxidation from accessing the Pt catalyst because the negatively charged niobate sheets repel triiodide anions. This finding subsequently led to the development of Z-schemes for overall water splitting using I^-/I_3^- shuttles for charge transfer between Pt loaded visible light-sensitized niobate reduction and WO_3-based O_2 evolution photocatalysts, the most efficient system of which is displayed in Figure 1.[22-24] The suppression of I_3^- back reaction at Pt by compartmentalization of the catalyst nanoparticles is critical for the efficiency of this system.

While the use of 2D metal oxide nanosheets affords blocking of specific undesired back or side reactions such as those involving charge transfer shuttles, the approach lacks designs for the rigorous blocking of crossover and back reaction of small molecules in general, such as O_2 generated at H_2O oxidation sites or intermediates of CO_2 conversion produced at reduction sites. Furthermore, the nanosheets lack the required proton permeability of artificial photosynthetic membranes.

Mimicking the natural photosystem, studies of ultrathin artificial soft materials such as lipid bilayers for the compartmentalizing photosynthetic functions were initiated decades ago.

Early examples are the spatial separation of organic electron donors from acceptors upon photo-induced charge separation [25] or the accumulation of proton gradients for driving an ATP synthase proton pump.[26,27] Most recently, an approach mimicking the thylakoid membrane was implemented in a metal-organic framework-based 2-photon Z-scheme for H_2O splitting to H_2 and O_2 in the form of a several nm thick liposome bilayer.[28] This biomimetic membrane uses randomly diffusing chemical shuttles for the transport of charges between the oxidizing and reducing metal-organic framework photocatalysts.

For an abiotic engineered solar fuel system, the fragile vesicle structures suitable for living cells need to be replaced by much more durable ultrathin materials. Similarly, approaches based on the liquid phase boundaries of biphasic solutions for suppressing undesired back charge transfer reactions,[29,30] which may be appropriate for specialty chemical syntheses, lack the durability and rigorous separation properties required for solar fuel generating systems.

3. Single graphene layer as photosynthetic membrane

Single layer graphene has emerged as a robust, atom-thick charge conducting 2D material [31,32] that blocks crossover of the smallest molecules including H_2 and even He atoms while possessing the ability to transmit protons (Figure 2a).[33,34] Hence, graphene sheets possess all required properties for an ultrathin separation membrane of an artificial photosystems. Specifically, they have the potential for use as efficient ohmic contacts between semiconductor or molecular photocatalysts for H_2O oxidation and CO_2 or H^+ reduction in 2-photon Z-scheme configuration while simultaneously functioning as H^+ transmitting and molecule separating membrane. Before discussing opportunities for developing complete nanoscale integrated

artificial photosystems with incorporated graphene membranes, quantitative aspects of charge and proton conductivity will be described, and the use todate of graphene as charge transfer component in photocatalytic systems summarized.

3.1 Transport properties of graphene

The metal-like charge conductivity and perfect gas blocking property under ambient conditions were established in the early days of graphene research,[35,36] while passage of protons through the material is a more recent finding. Specifically, crystallographically perfect single graphene sheets of 10^2 to over 10^3 μ^2 size, which are prepared by mechanical exfoliation of graphite crystals and free of pinholes, were found by standard conductitivity measurements to possess areal conductivity of 3 mS cm^{-2} when in contact with aqueous HCl solution or interfaced on both sides with Nafion exposed to saturated H_2O vapor at ambient temperature (experimental proton transport barrier E_a = 0.78 eV).[32,37,38] Importantly, illumination with visible light drastically boosts the proton conductivity if the graphene layer is in contact with metal nanoparticles that result in n-type doping of the graphene, such as Pt, Ni etc. Specifically, at low electrical bias (< 100 mV), illumination of the graphene layer with a solar simulator source (100 mW cm^{-2}) results in a 15-fold increase of the proton current density, which boosts the areal proton conductivity to 45 mS cm^{-2} without degradation of the integrity of the layer upon prolonged illumination.[39] The linear increase of the proton transport rate with increasing light intensity from sites of H_2O oxidation across the graphene layer (flat wavelength response throughout visible and near infrared regions) satisfies the increased demand for protons at catalytic CO_2 reduction sites on the opposing side of the graphene separation membrane. The enhanced H^+ conductivity is

explained by the development of a local photovoltage in the vicinity of metal nanoparticles due to transient hot electrons generated upon light absorption by the metal nanoparticles.[39]

It is interesting to note that single sheet graphene obtained by mechanical exfoliation of crystalline graphite is impermeable to any other types of ions,[37] and no proton permeability is observed for bi- and higher multilayer graphene, but only if each layer is defect-free.[33] On the other hand, graphene made by chemical vapor deposition features nanosized defects and shows areal H^+ conductivity as large as 4 S cm^{-2}.[40] It should be added that there are single sheet graphene analogues that exhibit higher proton conductivity than pristine graphene layers, like hexagonal boron nitride (1 S cm^{-2} at room temperature, E_a = 0.3 eV), but they lack charge conductivity.[33]

3.2 Graphene as ohmic contact for photocatalytic systems

Over the past decade, the ohmic property of graphene sheets has been exploited for boosting the efficiency of semiconductor based 2-photon Z-scheme systems for overall H_2O splitting as well as CO_2 reduction by H_2O (Figure 3a).[41-50] These breakthroughs were preceded by the observation of photoelectrocatalytic enhancement in 1-photon constructs when utilizing graphene as electron transfer mediator between semiconductor photocatalysts and electrode,[51] as efficient charge separator,[52] or as reduction co-catalyst.[53]

In this section, recent progress in engaging the excellent electron transfer property of graphene will be reviewed. The full membrane function of graphene that includes chemical separation and proton conductivity has not yet been exploited in the systems reported thus far.

The majority of these systems use few-layer thick graphene obtained by chemical or photochemical reduction of graphene oxide rather than structurally perfect single graphene layers

made by the mechanical exfoliation method.[54] Graphene oxide is synthesized by oxidation of graphite using chemical oxidants and typically adhered to the photocatalyst surface prior to reduction. The product of graphene oxide reduction (abbrev. RGO) features epoxy, hydroxyl, carbonyl and carboxylate groups at tens of percent concentration,[43,51] which are often accompanied by adjacent defects in the form Angstrom-sized holes in the graphene layer (Figure 2b).[55] While the reduction process removes a large fraction of O moieties as evidenced by XPS (X-ray photoelectron spectroscopy) and FT-IR (Fourier transform infrared) measurements (Figure 2d), the graphene defects remain (Figure 2c).[51] Prominent recent examples of water oxidation and H^+ reduction photocatalysts coupled by graphene are O_2-evolving $BiVO_4$ photocatalyst nanoparticles interfaced by RGO layers with H_2-evolving Ru doped $SrTiO_3$ nanoparticles, the latter decorated with Rh co-catalyst. The nanocomposite achieved a 3-fold increase in water splitting activity compared to particles with direct contact between $BiVO_4$ and $Ru/SrTiO_3$:Rh.[41] Similar efficiency enhancement was reported in subsequent studies that introduced RGO contacts for visible light Z-scheme constructs consisting of p-type metal sulfide for CO_2 (or H_2O) reduction (e.g. $CuGaS_2$) and n-type $BiVO_4$ decorated with CoO_x co-catalyst for O_2 evolution (Figure 3b).[44] In another example, the coupling of CdS nanoparticles for H_2O oxidation with $Fe_2V_4O_{13}$ platelets for CO_2 reduction by a graphene interface was found to substantially boost photocatalytic efficiency of this visible light driven heterostructure for the conversion of a gaseous CO_2 and H_2O mixture (Figure 3c).[45] Here, the graphene interface opens up efficient combination of CdS conduction band electrons with $Fe_2V_4O_{13}$ holes thereby enabling the Z-scheme mechanism.

While free standing graphene has a favorable Fermi level (-0.08 V vs. SHE)[56] for creating efficient ohmic contacts between photocatalytic materials for H_2O oxidation and H^+ or CO_2

reduction, it is nevertheless important to evaluate in each case the actual Fermi level upon interfacing the graphene sheet with photocatalytic materials in order to allow for graphene Fermi level modulation with the goal of minimizing the contact resistance for maximum photocatalytic efficiency. Specifically, the Fermi level of graphene should be lower (less reducing) than the conduction band minimum of the electron donor material but higher than the valence band maximum of the hole donor component, as illustrated by the ZnO-CdS Z-scheme.[49] This enables the graphene to efficiently accept the photoexcited electrons from ZnO and holes from CdS.

It is important to note that the use of graphene as electron transfer mediator is feasible not just for solid, but for molecular photocatalysts as well. For example, molecular light absorber-catalyst assemblies can be anchored on graphene sheets by aromatic moieties.[55,57] However, adequate areal density of molecular catalysts is critical for achieving practical photocatalytic rates for fuel generation. Therefore, charge conducting high surface area supports for molecular systems need to be introduced, as discussed in Sect. 5.

3.3 Single graphene layer as membrane for nanoscale integrated artificial photosystems

Because of their H^+ conducting and chemical separation properties on top of excellent charge conductivity, incorporation of single graphene sheets into artificial photosynthetic units offers the opportunity to block efficiency-degrading back reactions and drastically reduce charge and proton transfer distances. Sample constructs employed so far for evaluating H^+ conductivity of single graphene layers[33,39,58] provide a starting point for building complete, nanoscale integrated artificial photosystems featuring a graphene separation membrane. A single graphene sheet tightly covering a ~10 μ diameter hole etched through a Si wafer allows for facet-selective deposition of photocatalyst nanoparticles for H_2O oxidation on one side and CO_2 (or H^+)

reduction on the other side of the membrane (drop or spin casting, chemical vapor deposition),[45,57] enabled by the straightforward manipulation of the macro-sized Si wafer. To benefit from the large H^+ conductivity enhancement by illumination, metal nanoparticles need to be kept in contact with graphene on at least one facet. This could be achieved, for example, by using Ni co-catalyst nanoparticles for H^+ reduction or Cu nanoparticles for CO_2 reduction on the surface of semiconductor particles for photoreduction (contact with both Ni and Cu result in n-type graphene doping required for the enhancement of H^+ conductivity by light).[39,58] The deposited photocatalytic nanoparticles need to be separated by nano-sized spaces in order to maintain the H^+ conductivity across the membrane because semiconductor materials are typically proton impermeable. A proposed example of such a complete visible 2-photon tandem photosystem integrated on the nanoscale that features a graphene separation membrane would be $BiVO_4/CoO_x$ nanoparticles for H_2O oxidation on one side and $CuGaS_2$/Pt nanoparticles for H_2 evolution on the opposite side. The efficiency of this Z-scheme system was previously demonstrated in the form of an aqueous particle suspension using RGO as solid-state electron mediator.[44] Here, the Pt co-catalyst particles in direct contact with the graphene surface provides the H^+ conductivity-boosting effect upon photo-illumination.

In the case of Z-scheme systems for which one or both photocatalysts for the two half reactions are molecules, non-covalent attachment methods are preferred because they retain the high charge conductivity and chemical separation properties of graphene; this cannot be assumed for covalent attachment via functional groups introduced into graphene sheets. Favored non-covalent anchors are those providing strong π-π interactions such pyrene, naphthalene, perylene and other aromatic or heteroaromatic moieties.[57] However, such non-covalent attachment might be too weak to prevent detachment under sustained photocatalytic conditions. Furthermore,

monolayer coverage of molecular photocatalysts on graphene membranes provides far too low active site density for building systems whose catalytic rate can keep up with the photon flux at maximum solar intensity. Here, the recent emergence of charge conducting metal-organic frameworks (MOFs) and covalent-organic framework (COFs) provides high surface area supports for molecular photocatalytic assemblies suitable for developing viable photosystems using molecular components (Sect. 5).

4. Ultrathin amorphous silica with embedded molecular wires as photosynthetic membrane

Pinhole-free amorphous silica layers of several nm thickness prepared by atomic layer deposition (ALD) possess sufficient H^+ conductivity for serving as ultrathin separation membranes for artificial photosynthesis.[59] The required charge conductivity is enabled by a recently developed method for embedding organic molecular wires into such amorphous SiO_2 layers.[60,61] In this section, we discuss the synthesis and structure of SiO_2 nanolayers with embedded wires, followed by the quantitative evaluation of charge conductivity, H^+ conductivity, and chemical separation property. A complete nanoscale artificial photosynthetic unit in the form of an inorganic core-shell nanotube and a square inch-sized array of such nanotubes will be introduced that constitutes a macroscale photosynthetic system which retains the conductivity and separation property of the nanotubes.

4.1 Structure, conductivity, and separation property

Ultrathin conformal layers of amorphous silica provide robust separation barriers for small molecules. Recent studies have established adequate proton conductivity of such pinhole-free SiO_2 layers of a few nanometer thickness and found that they afford tight encapsulation of organic molecular wires for controlled charge transport.[59-61] This approach takes advantage of the high precision with which the structure and energetics of molecular systems can be manipulated for achieving maximum charge transfer efficiency. In the example illustrated in Figure 4a, the SiO_2-based, 3 nm thick membrane separates visible light photocatalysts in the form of heterobinuclear metal-to-metal charge transfer units (MMCT) for CO_2 reduction (Zr-O-Co^{II}) anchored on the SiO_2 surface from a H_2O oxidation catalyst, here Co_3O_4. Wires employed todate are oligo(*p*-phenylenevinylene) molecules with 3 aryl units (abbrev. PV3), with the length of the backbone commensurate with the thickness of the SiO_2 layer.[60-69] Through synthetic modification of the aryl or ethenyl moieties by electron donating or withdrawing groups, the HOMO (highest occupied molecular orbital) and LUMO (lowest unoccupied molecular orbital) energies of the wire molecules are fine-tuned in order to optimize the energetics of charge flow and impose rectifying property.[60,65] Figure 4b shows favorable energy level alignment of the HOMO of PV3 for spontaneous hole charge transfer from light absorber to Co_3O_4 catalyst while minimizing efficiency-degrading back reaction with the excited light absorber electron by the high negative potential of the wire LUMO, which is unable to be populated by the former.

The synthetic approach for embedding wire molecules of desired electronic properties, orientation and density into amorphous silica nanolayers involves a two-step assembly process. First, tripodal anchors in the form of trimethoxysilylaryl moieties are attached to the solid surface on one side of the membrane (in the example shown in Figure 4 to a Co oxide catalyst, but it could also be another solid material such as a semiconductor photocatalyst). This type of

anchor imposes vertical orientation upon subsequent covalent attachment of the PV3 wire by an amide bond or by click chemistry, thereby ensuring that the charge conducting molecules span the entire silica layer from one side to the other.[60,65,66] The free choice of the number of aryl rings allows for the accurate matching of wire length and silica thickness, while the chosen wire-to-anchor ratio determines the wire density. Casting of the wire molecules into amorphous silica by atomic layer deposition (ALD) close to room temperature results in tight encapsulation of the organic under preservation of its chemical integrity and spatial orientation. Moreover, the method keeps the separation property of the SiO_2 membrane intact, as verified by electrochemical measurements combined with surface-sensitive polarized Fourier-transform infrared reflection absorption spectroscopy (FT-IRRAS).[60,61,65,66]

4.1.1 Charge conductivity

For evaluating charge conductivity by photocurrent measurements, planar SiO_2 layers with embedded molecular wires were prepared on Co oxide nanolayers deposited on a planar Pt electrode (100 nm Pt e-beam evaporated onto Si wafer).[60] Accurate tuning of the density of the visible light absorber, here the familiar $Ru(bpy)_3$ (bpy = 2,2'-bipyridyl) photosensitizer with one of the three ligands modified for surface attachment, was accomplished by using the 2-step anchoring method discussed above for attachment to the silica membrane.[60,66] Short circuit photocurrent measurements using the three-electrode configuration shown in Figure 5a allowed us to quantify the charge flux through the membrane. Comparison of samples with and without embedded molecular wires but otherwise identical composition confirmed that charges are conducted exclusively through embedded wire molecules, and no degradation of the integrity of

the silica membrane upon exposure to photocurrent was noted. In particular, no pinholes developed as confirmed by control cyclic voltammetry (CV) experiments.[60]

Enhancing the charge flux across the membrane by optimizing the molecular wire density through photocurrent measurements for a wide range of loadings revealed a linear, approx. 10-fold increase from 0.5 to 4 nm^{-2} (Figure 5b). Quantitative determination of wire and light absorber densities of each sample was enabled by the combined use of FT-IRRAS and UV-vis spectroscopy.[60] The observed photocurrent increase with growing wire density reflects the enhanced electronic coupling and lowered reorganization energy that result from a shortened average spatial separation of anchored light absorber and terminal aryl ring of the embedded wire molecule.[70] A density around 5 nm^{-2} was found to be optimal since higher loadings compromise the integrity of the separation function of the silica membrane, mainly because the spaces between adjacent embedded wire molecules become too small for depositing adequate amounts of SiO_2.

A similarly steep enhancement of charge transfer across the ultrathin silica membrane was observed when optimizing the energy-level alignment of embedded molecular wire with light absorber and catalyst. By varying the HOMO potential of the embedded wire molecule using various electron donating or withdrawing substituents on the terminal aryl moiety (SO_3, F, OCH_3, selected based on HOMO potential estimates by DFT (density functional theory))[60] and alternate types of chemical bonding for wire attachment to tripodal anchors (amide, click linkage) displayed in Figure 6, the driving force (free-energy change) for charge hopping from light absorber to wire, and from wire to catalyst could be optimized (Figure 5c). These charge transfer steps were directly observed by ultrafast optical absorption spectroscopy.[69] A 10-fold increase of the photocurrent density was found upon replacement of an amide by a triazole

(click) linkage (Figure 5d), with the driving force of charge transfer from $Ru(bpy)_3$ light absorber to wire identified as the most influential parameter (Step 1, Figure 5c). While the observed photocurrents for the systems shown are still mere tens of nA cm^{-2}, replacing the initially used persulfate electron acceptor in solution that activates the photoexcited light absorber by a much more efficient solid oxide electron acceptor, here the conduction band of a TiO_2 nanolayer, affords photocurrents as high as 6.4 μA cm^{-2}. This result pertains to the comparatively inefficient amide-linked wire and as yet un-optimized wire density.[60] Therefore, if replaced by the most efficient click-attached wire at optimal density of 5 nm^{-2}, a photocurrent of 0.1 mA cm^{-2} can be achieved. The current density for planar geometry is adequate for reaching the 10 mA cm^{-2} target for an artificial photosystem [71] because of the high surface area of its nanostructured architecture, as will be discussed in Sect. 4.2. Similar to the optimization of the HOMO potential of the wire molecules for hole conduction, matching of the LUMO for optimal electron transfer via embedded wire molecules to catalytic reduction sites was achieved by introducing strongly electron-withdrawing NO_2 and CN substituents on aryl and ethenyl backbone moieties.[65]

4.1.2 Proton conductivity

Using planar amorphous SiO_2 layers of variable thickness in the few nm range prepared by ALD on Pt electrodes, the proton transport resistance was determined by electrochemical impedance spectroscopy (EIS). The measurement method is based on monitoring of the reduction of H^+ transferred through the silica layer to hydrogen (i.e. Pt-H) upon arrival at the SiO_2/Pt interface at potentials short of the onset of H_2 evolution (termed H under potential deposition (abbrev. H_{upd})).[72] As shown in the cyclic voltammograms (CV) of Figure 7a, sweeps in N_2-saturated aqueous solution at pH 4 reveal cathodic current in the range 0.4 to 0 V (vs. RHE) originating

from the reduction of H^+ to Pt-H. The formation of the latter, and its Pt-D counterpart in D_2O, were spectroscopically verified by accompanying FT-IRRAS measurements (2090 and 1470 cm^{-1}, respectively).[59] By holding the potential at V_{upd} = 0.096 V vs. RHE, EIS measurements gave H^+ transport impedance values that reflect a modest conductivity of 4 x 10^{-8} S cm^{-1} (Figure 7b),[59] which agrees with literature values for μ thick amorphous silica when extrapolated to room temperature. Yet, due to the ultrathin nature of the layer, H^+ fluxes of 4900, 1900, and 1250 s^{-1} nm^{-2} were achieved for 2, 4, and 6 nm layers, respectively, when exposed to pH 4 aqueous solution.[59,61] These flux values range from close to matching, to greatly exceeding the photon flux at maximum solar intensity of 1500 s^{-1} nm^{-2}.[73]

At the same time, silica ALD layers as thin a 2 nm completely block crossover of molecules as small as O_2, as demonstrated by the fact that the characteristic O_2 reduction wave of bare Pt exposed to O_2-saturated is absent in the CVs of any of the ultrathin SiO_2 layers (Figure 7c). Like in the case of O_2-free solution, only the H_{upd} currents are observed. The H^+ conductivity and O_2 blocking properties are preserved in the presence of embedded wire molecules.[65] These results establish ultrathin silica layers with embedded wires as separation membranes based on which nanoscale artificial photosystems can be developed.

The mechanism of H^+ diffusion through conformal silica layer is understood as H^+ hopping according to the Grotthuss mechanism in which H^+ ions transiently bind and dissociate from O atoms (Si-O-Si bridges, SiOH or SiO^- moieties) throughout the interior of the solid.[74-76] The hopping mechanism is consistent with the low activation barrier for H^+ diffusion of 5 kcal mol^{-1} derived from our data, which agrees well with ab initio calculations.[59,77] It is important to add that H^+ transfer across the interfaces between the SiO_2 membrane and adjacent Co_3O_4

catalyst, or other metal oxide layers, is facilitated by interfacial Si-O-Co bridges uncovered by the FT-IRRAS technique.[59]

4.2 Ultrathin silica membranes for developing nanoscale integrated artificial photosystems

The synthetic methods developed for silica nanomembranes are suitable for any morphology and, hence, open up the development of complete nanoscale artificial photosystem with suitable geometry for the separation of the incompatible CO_2 reduction and H_2O oxidation environments. Moreover, the flexible choice of the morphology for the nanoscale units allows for their assembly into macroscale photosystems (~square inch) in a manner that preserves the separation of the H_2O oxidation and CO_2 reduction environments already achieved at the nanoscale. A specific example is tube morphology for the nanoscale photosynthetic unit that forms the basis of our integrated systems design, graphically sketched in Figure 8a. A core-shell nanotube consisting of a Co_3O_4 inner tube of about 10 nm thickness (core) is surrounded by a 3 nm thick SiO_2 membrane with embedded wires (shell). Visible light absorbing photocatalysts for CO_2 reduction, here robust ZrOCo MMCT units, are attached to the outside silica membrane surface. A cross-sectional HR-TEM image of the wall of a single nanotube is shown in Fig. 8b. Transient Zr^{III} generated by the separation of positive and negative charges upon photoexcitation of $Zr^{IV}OCo^{II}$ groups reduces vapor phase CO_2 to CO on the outside of the tube.[61,62,78-82] The hole charge on transient Co^{III} is transferred to Co_3O_4 via embedded molecular wires, driving H_2O vapor oxidation to O_2 on the inside of the tube.

Assembling such core-shell nanotubes, each independently driving photo-conversion of CO_2 and H_2O vapor to CO and O_2 under membrane separation, into arrays of square-inch size as schematically shown Figure 8c provides extension of the product separation from the nano- to

the macroscale.[61,81] A section of the nanofabricated array is shown in the scanning electron microscopic (SEM) image of Figure 8d. The fabrication process is based on a sacrificial Si nanorod templating technique and combines ALD of the various inorganic oxide layers with the wire functionalization protocol first optimized for planar samples, as described above.[83] By adding a top and bottom cover to the array with the tube opening piercing through them as discussed in Sect. 6, the O_2 gas evolving inside the nanotubes escapes into the surrounding atmosphere and is spatially completely separated from the CO_2 reduction sites and evolving fuel generated in the gallery space between the two covers.[61,81,83] The 100-fold larger surface area of the nanotube array when compared to its footprint allows for adequate density of light absorber and catalytic sites such that the photocatalysis rate can keep up with the solar photon flux (10 mA cm^{-2} electron flow density, $\geq$ 1 S cm^{-2} areal proton conductivity). Thus, the ultrathin SiO_2 membrane possesses the required properties for an efficient separation membrane for nanoscale integration of artificial photosystems. It is important to add that for optimizing overall conversion efficiency for CO_2 photoreduction by H_2O, the single light absorber systems investigated thus far need to be replaced by a 2-photon Z-scheme light absorber system, rendered feasible by the hierarchical nature of the assembly of core-shell nanotubes. It can be achieved by introducing two binuclear light absorbers with complementary optical properties and matched redox potentials, coupled in tandem by SiO_2-embedded wire molecules with properly aligned HOMO and LUMO energetics.

5. Electron and proton conducting 2D metal-organic and covalent organic frameworks as molecular photocatalyst supports

While a variety of atomically and molecularly precise deposition techniques are available for the coupling of heterogeneous photocatalysts to graphene or ultrathin silica-based membranes for building nanoscale artificial photosystems, coupling of molecular photocatalytic components to such membranes for adequate photocatalytic activity poses a special challenge.[84] Sufficiently large catalytic rates for keeping up with the solar photon intensity typically require much higher areal catalyst concentrations than afforded by monolayer coverage of flat surfaces. Yet, exploring systems based on molecular catalysts is attractive because of the comparative ease and precision of tuning of the electronic and chemical properties by synthetic manipulation, which is the key for maximizing efficiency and product selectivity. Therefore, high surface area nanoporous layers of tens of nm thickness that possess adequate electron and proton conductivity are needed.

The recent development of 2D metal-organic frameworks (MOFs) and 2D covalent organic frameworks (COFs, the metal-free variants) with appropriate electron and proton conductivity presents opportunities for addressing this challenge. Molecular electrocatalysts can be incorporated into the framework thereby allowing for high areal catalyst density and, hence, desired electrochemical activity.[84-86] These types of frameworks were first mainly explored as molecularly defined, high surface area porous solids for the selective adsorption of small gaseous molecules including CO_2 or H_2 for the purpose of storage, or for serving as separation membrane.[87-92] For the latter application, ultrathin MOF and COF membranes of tens of nm thickness have recently been developed.[93] As such, MOFs and COFs are typically electric insulators. Thus, methods needed to be explored for introducing electron (or hole) conductivity into the framework, and for enhancing the capacity of transporting protons.

After discussing recent progress in charge and proton conducting metal- and covalent organic frameworks, this section will describe the current status of electrocatalytic MOFs for H_2O splitting and CO_2 reduction. As such, MOFs and COFs are not suitable as separation membranes of artificial photosystems because they do not block small molecules (H_2O, O_2, small hydrocarbons intermediates and products). Thus, opportunities for integrating these frameworks with graphene membranes will be discussed.

5.1 Electron and proton conductivity of metal-organic frameworks

Charge conduction in MOFs can occur through covalent linkages of coordination polymers that constitute the porous framework (through-bond mechanism), pairing of transition metals with ligands containing chelating functional groups (extended conjugation mechanism), non-covalent interactions (through-space mechanism), or electron transfer guest species loaded into the pores (guest-promoted charge transport).[85,86] Early examples for conductive MOFs based on the hopping-type through-bond approach are frameworks using metal bis(dithiolene) moieties, with the covalency of the metal-sulfur bonds being a critical factor (conductivity around 10^{-4} S cm^{-1}).[94] Very high conductivities were achieved more recently with Fe-based MOFs (mixed-valence $Fe^{2+/3+}$) featuring azolate ligands (range 10^{-3} – 1 S cm^{-1}) (Figure 9a and 9b).[95-98] Particularly favorable as electron conducting ultrathin MOFs are those with extended conjugation because their π-d conjugation imparts efficient charge delocalization, hence exceptional conductivity in the plane of the 2D transition metal-chelating ligand structure (e.g. aromatic diols, diamines, dithiols). At the same time, non-covalent π-π interactions between the stacked planes assure good conductivity in the perpendicular direction. The through-space conductivity of planar conjugated organic ligands enabled by π-π interactions (e.g. tetrathiafulvalene, naphthalene-, anthracene, and

naphthalenediimide) offers exquisite control by fine-tuning of the stacking structure and of intermolecular distances provided by the highly ordered MOF architectures. The first cases of MOFs with through-space conductivity featured π-π stacked tetrathiafulvalene tetrabenzoate ligands of Mn, Co, Zn or Cd complexes that give rise to conductivities in the 10^{-6} to 10^{-4} S cm^{-1} range.[99,100] Recently reported MOF of $Cu_3(HOTP)_2$ (HOTP = hydroxytriphenylene) (Figure 10a) and $Ni_3(HITP)_2$ structure (Figure 10b) reach very high conductivities of 1 S cm^{-1} and 40 S cm^{-1}, respectively, with the latter serving as efficient O_2 evolving electrocatalyst.[101,102]

In addition to the pathways mentioned so far, all featuring charge transfer moieties as part of the framework, the space provided by the pores themselves can be utilized for introducing extrinsic electroactive species to engineer charge transfer conduits (guest-promoted transport). Electron (or hole) hopping between guest species at high loading, or between guest and framework moieties, can impart conductivity over a wide range (10^{-8} – 1 S cm^{-1}).[85] Typical electroactive guest species are I_2/I^- and polyiodides, aromatic (e.g. tetracyanoquinodimethane, methylviologen, C_{60}) or organometallic species (e.g. metallocenes) that undergo charge transfer to framework moieties. Limits of this approach are reduced porosity that might impair reactant and/or product transport through the MOF. Also, conductive polymers or 1D metal oxide chains have been synthesized from monomeric precursors inside MOF channels, resulting in embedded wire-like structures that resemble the embedded wire silica membranes discussed in Sect. 4. Such materials include 2D layers as thin as 10 nm or less with good electron conductivity.[103-105]

Regarding proton conductivity, the high versatility of introducing tailored functionalities into the framework or accommodating as guest molecules in the pores for boosting proton concentration and mobility has been increasingly exploited in the past 10 years. This effort was driven in part by the need for new types of proton exchange membranes for solid electrolyte fuel

cells.[106-108] Proton conductivities in the range 10^{-4} to 10^{-2} S cm^{-1} were recently reported for both humid and anhydrous reaction conditions[106] exceeding by orders of magnitude the conductivity required for keeping up with catalysis rates at maximum solar photon flux. Given the wide range of synthetic modifications available for organic framework components, it is reasonable to assume that adequate proton conductivity can be achieved by additional modification of practically any MOF or COF with favorable electrical conductivity and catalytic property.

5.2 MOF supported molecular electrocatalysts for artificial photosynthesis

A growing effort in the development of MOFs and COFs for electrocatalysis for energy that takes advantage of charge and proton conductivity includes systems for H_2 evolution,[84,109-111] H_2O oxidation,[112-116] O_2 reduction,[102] and CO_2 reduction.[117-120]. The areal density of Co dithionene, a H_2 producing molecular catalyst supported on a charge conducting triphenylene hexathiol-based MOF was found to be 2 orders of magnitude higher than for the same molecular catalyst anchored on a flat surface.[84] Similarly, a MOF featuring Fe porphyrin CO_2 reduction catalyst as linkers was determined by chronoamperometry to afford a 1000-fold increase in areal density of electrically addressable, catalytically active sites compared to monolayer coverage of a flat electrode surface. The Fe porphyrin linkers serve both as redox-hopping conduits and catalytic sites, with the rate of electron diffusion through the MOF limiting the catalysis rate in this case[119] (it is interesting to note that when the photoelectrocatalytic linker is introduced at too low density, it is the electron transfer through the MOF which limits the photocatalytic efficiency).[115] The well-established CO_2 reduction catalyst Co phthalocyanine octaol was incorporated into the framework as a tetratopic linker, which resulted in high electrocatalytic activity enabled by the proton and electron conductivity of metal-catecholate MOF framework.

This Co phthalocyanine Fe catecholate MOF exhibits 16.5 mA cm^{-2} catalytic current density for CO_2 reduction to CO (V_{RHE} = -0.63 V, overpotential 0.52 V), which is 10 times higher than non-conductive MOFs featuring porphyrin catalysts with similar TOF as Co phthalocyanine.[107,120] Utilizing the charge mobility enabled by π conjugation and π-π stacking, COFs featuring a Co porphyrin catalyst incorporated into the framework achieved a 26-fold improvement of the electrocatalytic CO_2 to CO conversion compared to free molecular catalyst.[118] In a related system, a Co porphyrin as part of a MOF featuring $Al_2(OH)_2$ backbone allowed the electrochemical conversion of CO_2 to CO at high selectivity. UV-vis spectroelectrochemical measurements directly demonstrated the electrical connectivity of the vast majority catalytic metal centers of this MOF. It is important to note that for MOF film thicknesses of hundreds of nm and larger, the fraction of electrochemically accessible Co sites decreases rapidly with increasing thickness as electron and proton transfer becomes hindered, rendering 2D MOF thicknesses in the range from tens of nm to about 200 nm optimal.[111,117]

Exploiting the synergistic catalytic effect of two different metal centers electronically coupled in the framework, a remarkably high electrocatalytic current density for O_2 evolution of 10 mA cm^{-2} at 189 mV overpotential was achieved for NiCo benzenedicarboxylic acid based 2D MOF in alkaline solution (pH 14) whose structure and polarization curves are shown in Figure 11a and 11b, respectively.[112] Even further reduction of the overpotential for water oxidation was recently achieved with other bi- and trimetallic MOF electrocatalysts.[121,122]

5.3 Integration of molecular catalyst-loaded 2D MOFs and COFs with ultrathin separation membrane for nanoscale artificial photosystems

For molecular catalyst based artificial photosystems that take advantage of the high loading density achievable by incorporation into 2D MOFs or COFs, two possible configurations are envisioned for integration with a graphene separation membrane. In one configuration, the MOFs would feature both the light absorption and the catalytic function in the form of molecular linkers or metal nodes, with the photocatalytic MOF for H_2O oxidation forming an interface on one side of a graphene membrane and the photocatalytic MOF for CO_2 (or H^+) reduction on the opposite side akin to a recently reported construct consisting of a graphene sheet sandwiched between thin nanoporous silica layers on either side, sketched in Figure 12a.[123] A variety of synthetic approaches for interfacing MOFs with graphene have been demonstrated and comprehensively reviewed, with an example illustrated in Figure 12b.[124-126] For the H_2O oxidation half reaction, transient hole charges generated upon light absorption drive the O_2 evolution catalyst inside the MOF while the excited electrons are transferred to the graphene interface. According to the Z-scheme mechanism, the electrons combine with holes generated in the fuel-forming photoreductive MOF on the opposite side of the graphene membrane. A variant of this configuration may additionally feature semiconductor metal oxide nanolayers inserted between the graphene layer and the MOFs: The MOF on each side is deposited onto an appropriate large bandgap oxide nanolayer according to established methods [127] that serves as electron (hole) conduit to the ohmic graphene interface. For example, a NiO nanolayer could serve as hole acceptor of the photoreductive MOF and a TiO_2 layer as electron acceptor of the H_2O oxidation MOF, with the graphene sandwiched between the two metal oxide nanolayers. This variant is reminiscent of molecular photocatalyst-NiO photocathode and analogous TiO_2 photoanode assemblies developed by the groups of Meyer [128,129] and Wasielewski.[130]

An alternate configuration of a MOF-based nanoscale artificial photosystem might be composed of a semiconductor Z-scheme for visible light absorption and charge separation featuring a sandwiched graphene separation membrane as ohmic contact, and 2D MOFs with incorporated molecular oxidation and reduction catalysts deposited on opposite sides of the semiconductor construct. As an example, the photocatalytic system could consist of a visible 2-photon tandem semiconductor unit for efficient solar light absorption such as GaAs/graphene/Si, with a MOF for H_2O oxidation deposited on the Si surface and a MOF for CO_2 (or H^+) reduction on the GaAs surface using techniques established for other III-V semiconductor surfaces.[131] For maximum photocatalytic efficiency, a critical property to optimize will be the energy level alignment of the electron and valence band edges of the tandem semiconductor unit with the respective potentials of the electron and hole transfer conduits of the MOFs. Furthermore, the samples should be made in the form of nanoparticle films with free, uncovered nano-sized graphene spaces in between to ensure adequate proton flux because semiconductor materials are typically proton impermeable.

6. Conclusions and Outlook

Ultrathin charge and proton transmitting membranes of ~10 nm thickness capable of separating O_2, H_2O, CO_2 and small carbon-based molecules open up opportunities for developing complete nanoscale integrated artificial photosystems to overcome efficiency limitations of existing integrated systems based on traditional, orders of magnitude thicker membranes. Graphene and ultrathin amorphous silica with embedded molecular wires possess the required membrane properties for enabling the exploration of both solid and molecular photocatalyst integration. In

addition to chemical separation, the efficiency of electron (hole) and H^+ transport are critical for the development of nanoscale integrated solar fuel systems. Recent progress in the quantitative assessment of these transport properties described in this article provides guidance for designing assemblies for the incorporation of nanoscale photosynthetic units into efficient macroscale photosystems.

A critical task of developing macroscale artificial photosystems based on the nanoscale integrated units is to retain the membrane separation of the catalytic oxidation sites and the evolving O_2 from the reduction sites and the emerging fuel product on all length scales from nanometer up to inch-sized units and beyond. For semiconductor nanoparticulate Z-scheme tandem light absorbers featuring graphene ohmic contact and metal (or metal oxide) co-catalysts on either side, a possible approach is to replace the perforated Si wafer referred to in Sect. 3 with a free standing inch-sized porous (~1-10μ) silica or alumina support. Each pore would be covered by a graphene sheet decorated with the nanoparticle photocatalysts, shown in Figure 12c in the form of nanorods. In this way, the membrane separation of the catalytic half reactions and evolving products would extend to the macroscale. Both silica and alumina supports are known to provide adequate adhesion of the graphene layers by van der Waals forces between exfoliated single graphene and the oxide surface to withstand the development of leaks.[33] For MOF-supported molecular light absorber/catalyst systems with a graphene membrane serving as ohmic contact of the Z-scheme, whose nanoscale integration is outlined in Sect. 5, a similar macroscale construct may be feasible. Here, continued improvement of the efficiency of electron (or hole) transfer through the frameworks by fine tuning of the MOF electronic states is another urgent task to pursue.

Whether a single such square inch sheet exposed to sunlight is adequate for productively utilizing the majority of the impinging photons at maximum intensity, or whether a stack of multiple sheets is required, will depend mainly on two factors. One is the loading density of photocatalyst nanoparticles (or molecular photocatalysts), the other is the areal H^+ conductivity of the graphene. As mentioned in Sect. 3, RGO sheets typically feature a sufficient density of defects such that the sheet sustains an areal H^+ conductivity of 1 S cm^{-2} or higher. Defect-free single graphene sheets have areal H^+ conductivity around 0.05 S cm^{-2}, which requires up to 20 stacked sheets for sustaining adequate H^+ flux under maximum solar irradiation. In this case, sheet facets would be oriented such that the reactant spaces between the sheets would alternate between O_2 evolution and fuel production.

For assemblies of Co oxide-silica core-shell nanotube photosynthetic units featuring ultrathin silica membranes with embedded molecular wires, square inch sized nanotube arrays (Figure 8) provide one approach for extending the product separation from the nano to the macroscale. Completion of the nanotube array by installing a top and bottom cover plate with the nanotube opening piercing through them, as pictured in Figure 12d, requires replacement of the sacrificial Si nanorod template approach by the anodized aluminum oxide (AAO) method.[132-139] The use of AAO as sacrificial template for growing core-shell nanotube arrays by ALD is well established.[134,137,138] Installation of top and bottom SiO_2 covers of the nanotube array involves sequences consisting of selective partial AAO etching, temporary protection by organic fillers, silica ALD, and mechanical polishing as previously demonstrated for the fabrication of various nanotube and nanorod arrays.[132,137,139] The flexibility of the AAO method for tuning tube diameter, length and pitch, CO_2 and H_2O gas flow and photocatalysis product desorption as well

as photonic properties will allow optimization of the system for maximum sunlight to fuel conversion efficiency.

Beyond graphene and silica, continued exploration of inorganic 2D materials as ultrathin membranes for artificial photosystems is important. An example is the broad class of 2D charge conducting MXenes, for which exploration of their potential for adequate H^+ conductivity is a next task to pursue.

Conflicts of Interest

There are no conflicts of interest to declare.

Acknowledgement

This work was supported by the Director, Office of Science, Office of Basic Energy Sciences, Division of Chemical, Geological and Biosciences of the US Department of Energy under contract no. DE-AC02-05CH11231. Funding for support of the work on ultrathin silica membranes was in part provided by the Energy and Biosciences Institute through the EBI-Shell program.

Figure Captions:

Figure 1: Z-scheme tandem system for visible light driven overall water splitting using Al_2O_3 modified niobate nanosheets with Pt nanoparticle catalyst for H^+ reduction compartmentalized in interlayer spaces and I^-/I_3^- as electron transfer shuttle. Efficiency enhancement is achieved by blocking access of I_3^- to Pt by electrostatic repulsion of the negatively charged niobate sheets. Reproduced from ref. 23 with permission from the American Chemical Society, Copyright 2020.

Figure 2: Graphene. **(a)** Defect-free single graphene layer. **(b)** Graphene oxide. **(c)** Reduced graphene oxide (RGO). Reproduced from ref. 34 with permission from John Wiley & Sons, Copyright 2019. WILEY-VCH Verlag GmbH & Co. KGaA, Weinheim. **(d)** Carbon (1s) XPS of graphene oxide before (top) and after reduction by visible light excitation of $BiVO_4$ photocathode for 3 h (bottom). The C-O (epoxy and hydroxyl, 286.6 eV) and carboxylate C=O (288.9 eV) show a sharp decrease while the C-C signal (284.5 eV) increases. Reproduced from ref. 51 with permission from the American Chemical Society, Copyright 2018.

Figure 3: Graphene serving as ohmic contact of Z-scheme tandem photosystems. **(a)** Ohmic contact enabling charge flow of TiO_2-Si Z-scheme heterostructure for photocatalytic H_2O splitting. The photogenerated electrons in Si and holes in TiO_2 move to aqueous interface to perform water splitting, while the holes in Si and electrons in TiO_2 recombine at the ohmic contact between the two semiconductors. Reproduced from ref. 50 with permission from the American Chemical Society, Copyright 2013. **(b)** Photosystem for H_2O splitting with graphene contact between $BiVO_4$-CoO_x oxidation and CuGaS -Pt reduction photocatalysts. Reproduced

from ref. 44 with permission from the American Chemical Society, Copyright 2016. **(c)** Photosystem for CO_2 reduction by H_2O with graphene contact between CdS oxidation and $Fe_2V_4O_{13}$ reduction photocatalyts. Reproduced from ref. 45 with permission from the Royal Society of Chemistry.

Figure 4: Ultrathin amorphous silica membrane with embedded molecular wires. **(a)** Schematic of visible light driven hole transfer from transient Co^{III} formed by $Zr^{IV}OCo^{II} \rightarrow Zr^{III}OCo^{III}$ charge transfer photoexcitation via embedded molecular wire to Co_3O_4 catalyst. Reproduced from ref. 62 with permission from the American Chemical Society, Copyright 2018. **(b)** Energy level alignment of light absorber, PV3 wire, and catalyst for light-induced directional charge transfer for driving H_2O oxidation and CO_2 reduction. Oxidation and reduction catalysis occurs at the gas/solid interface, with an H^+ gradient developing across the nanomembrane during photocatalytic H_2O oxidation. The SiO_2 membrane blocks crossover of reactants and products, except for H^+. Adapted from ref. 82 with permission from the Royal Society of Chemistry.

Figure 5: Short circuit photocurrent measurements for assessing electron conductivity. **(a)** Schematic of three-electrode cell with working Pt electrode onto which 12 nm Co_3O_4 followed by 3 nm silica membrane with embedded TMS-Am-PV3-SO_3 wires are deposited. Covalently anchored $[Ru(bpy)_2(dcbpy)]^{2+}$ light absorbers are also shown. **(b)** Wire density dependence of photocurrent. **(c)** Energy level alignment of the HOMO of molecular wires with the HOMO of Ru light absorber and Co_3O_4 catalyst valence band. Anchored wires are abbreviated OMe for E-PV3-OMe, SO_3Et for E-PV3-SO_3Et, F_5 for E-PV3-F_5, and SO_3 for A-PV3-SO_3. The corresponding molecular structures are shown in Figure 6. **(d)** Photocurrent dependence on the

HOMO potential of the embedded wire molecule, normalized for wire density of 0.6 nm^{-2}. Reproduced from ref. 60 with permission from the American Chemical Society, Copyright 2021.

Figure 6: Functionalized wire molecules with electron-donating and -withdrawing groups. **(a)** Free wires. **(b)** Wires attached to anchor by amide or triazole linker. Corresponding HOMO potentials of wire linked to the anchor (vs. NHE) are shown in schematic Figure 4c. Reproduced from ref. 60 with permission from the American Chemical Society, Copyright 2021.

Figure 7: Proton conductivity and O_2 blocking property of ultrathin silica membrane. **(a)** Cyclic voltammogram (CV) of bare Pt electrode (black trace) and Pt covered with 2, 4, and 6 nm SiO_2 (red, blue, and green traces) at 298 K in N_2-saturated aqueous 0.5 M Na_2SO_4 solution at pH 4. **(b)** Electrochemical impedance spectra in N_2-saturated pH 4 electrolyte solution used for (a). Applied potential 0.096 V vs. RHE. The dots in the plot are the experimental data and the solid lines represent the results of fitting the data to the equivalent circuit (Randles circuit) shown in the inset. **(c)** CV in O_2-bubbled electrolyte solution under the same conditions as used for (a). Reproduced from ref. 59 with permission from John Wiley & Sons, Copyright 2019. WILEY-VCH Verlag GmbH & Co. KGaA, Weinheim.

Figure 8: Co oxide-silica core-shell nanotube featuring a silica nanomembrane as complete photosynthetic unit for CO_2 photoreduction by H_2O. **(a)** Schematic of design. **(b)** HR-TEM image showing a longitudinal cross-section of a single Co_3O_4-SiO_2 core-shell nanotube wall. Inset: fast Fourier transform (FFT) image of the crystalline Co_3O_4 layer. Reproduced from ref. 83 with permission from the American Chemical Society, Copyright 2018. **(c)** Schematic of core-

shell nanotube array. **(d)** SEM of section of macroscale $Co_3O_4/SiO_2/TiO_2$ nanotube array after complete removal of sacrificial Si template. Reproduced from ref. 61 with permission from the Royal Society of Chemistry.

Figure 9: Highly electron conductive mixed-valence Fe azolate MOFs. **(a)** Iron tetrazolate MOF crystal structure (left) and $(Fe\text{-}N\text{-}N)_\infty$ chains serving as charge transport conduits (right). Fe, green dots; N, blue dots. Reproduced from ref. 96 with permission from the American Chemical Society, Copyright 2018. **(b)** Structure of secondary building unit of MOF Fe(1,2,3-triazolate)$_2(BF_4)_x$ (left) and Fe-N sublattice (right). Reproduced from ref. 98 with permission from the American Chemical Society. Copyright 2018.

Figure 10: Highly conductive two-dimensional MOFs. **(a)** 2D honeycomb layers of $Cu_3(HOTP)_2$ with square planar Cu centers bridging triphenylene-based linkers (top). Continuous slipped stacking arrangement of $Cu_3(HOTP)_2$ layers providing π-π interaction is also shown (bottom). Reproduced from ref. 101 with permission from the American Chemical Society, Copyright 2019. **(b)** Two-dimensional layered structure of $Ni_3(HITP)_2$ MOF. Reproduced from ref. 102 with permission from Springer Nature, Copyright 2016.

Figure 11: Ultrathin bimetallic NiCo MOF for electrocatalytic O_2 reduction. **(a)** MOF crystal structure. **(b)** Polarization curves of bimetallic NiCo MOF (dark blue trace) compared with monometallic Ni (red), Co (light blue), RuO_2 (purple) and bulk NiCo MOF (black). Reproduced from ref. 112 with permission from Springer Nature, Copyright 2016.

Figure 12: Proposed designs of using ultrathin conductive separation membranes for nanoscale integrated photosystems. **(a)** Schematic of graphene membrane sandwiched between nanoporous silica layers of tens of nm thickness with vertically aligned pores. Reproduced from ref. 123 with permission from John Wiley & Sons, Copyright 2017. WILEY-VCH Verlag GmbH & Co. KGaA, Weinheim. **(b)** MOF of structure $Zr_6O_4(OH)_4(bdc\text{-}NH_2)_6$, $bdc\text{-}NH_2$ = 2-amino-1,4-benzenedicarboxylate (blue/yellow) interfaced with graphene membrane (red). Reproduced from ref. 124 with permission from the American Chemical Society, Copyright 2022. **(c)** Section of array of semiconductor particle Z-scheme, here in the form of nanorods, with graphene sheet serving as ohmic contact of photoanode/cathode and as proton transmitting separation membrane. Portion of figure adapted from ref. 136 under Creative Commons license http://creativecommons.org /licenses/by/4.0/. **(d)** Complete Co oxide - silica nanotube array with top and bottom cover for permanent separation, on all length scales, of evolving CO_2 reduction product (gallery space between the top and bottom covers) and O_2 (inside tubes and external space). Reproduced from ref. 82 with permission from the Royal Society of Chemistry.

References

[1] IPCC, 2022: *Climate Change 2022: Mitigation of Climate Change. Contribution of Working Group III to the Sixth Assessment Report of the Intergovernmental Panel on Climate Change*. P. R. Shukla, J. Skea, R. Slade, A. Al Khourdajie, R. van Diemen, D. McCollum, M. Pathak, S. Some, P. Vyas, R. Fradera, M. Belkacemi, A. Hasija, G. Lisboa, S. Luz and J. Malley, eds. Cambridge University Press, Cambridge, UK and New York, NY, USA.

[2] S. Y. Reece, J. A. Hamel, K. Sung, T. D. Jarvi, A. J. Esswein, J. J. H. Pijpers and D. G. Nocera, *Science*, 2011, **334**, 645-648.

[3] E. Verlage, S. Hu, R. Liu, J. R. Jones, K. Sun, C. Xiang, N. S. Lewis and H. A. Atwater, *Energy Environ. Sci.*, 2015, **8**, 3166-3172.

[4] K. Sun, R. Liu, Y. Chen, E. Verlage, N. S. Lewis and C. Xiang, *Adv. Energy Mater.*, 2016, **6**, 1600379.

[5] J. L. Young, M. A. Steiner, H. Doescher, R. M. France, J. A. Turner and T. G. Deutsch, *Nat. Energy*, 2017, **2**, 17028.

[6] F. F. Abdi, L. Han, A. H. M. Smets, M. Zeman, B. Dam and R. van de Krol, *Nat. Commun.*, 2013, **4**, 2195.

[7] W. H. Cheng, M. H. Richter, I. Sullivan, D. M. Larsen, C. Xiang, B. S. Brunschwig and H. A. Atwater, *ACS Energy Lett.*, 2020, **5**, 470-476.

[8] C. Liu, J. Tang, H. M. Chen, B. Liu and P. Yang, *Nano Lett.*, 2013, **13**, 2989-2992.

[9] J. Luo, J. M. Im, M. T. Mayer, M. Schreier, M. K. Nazeeruddin, N. G. Park, S. D. Tilley, H. J. Fan and M. Graetzel, *Science*, 2014, **345**, 1593-1596.

[10] X. Zhou, R. Liu, K. Sun, Y. Chen, E. Verlage, S. A. Francis, N. S. Lewis and C. Xiang, *ACS Energy Lett.*, 2016, **1**, 764-770.

[11] W. H. Cheng, M. H. Richter, M. M. May, J. Ohlmann, D. Lackner, F. Dimroth, T. Hannappel, H. A. Atwater and H. J. Lewerenz, *ACS Energy*, 2018, **3**, 1795-1800.

[12] N. A. Campbell, J. B. Reece, M. R. Taylor and E. J. Simon, *Biology: Concepts & Connections*, Educational Pearson, New York, 5th edn., 2006.

[13] R. E. Blankenship, M. T. Madigan and C. E. Bauer, eds., *Anoxygenic Photosynthetic Bacteria*, Kluwer Academic, Dortrecht, 1995.

[14] S. Chabi, K. M. Papadantonakis, N. S. Lewis and M. S. Freund, *Energy Environ. Sci.*, 2017, **10**, 1320-1338.

[15] S. L. McFarlane, B. A. Day, K. McEleney, M. S. Freund and N. S. Lewis, *Energy Environ. Sci.*, 2011, **4**, 1700-1703.

[16] J. M. Spurgeon, M. G. Walter, J. Zhou, P. A. Kohl and N. S. Lewis, *Energy Environ. Sci.*, 2011, **4**, 1772-1780.

[17] K. Domen, A. Kudo, A. Shinozaki, A. Tanaka, K. Maruya and T. Onishi, *J. Chem. Soc., Chem. Commun.*, 1986, 356-357.

[18] A. Kudo, A. Tanaka, K. Domen, K. Maruya, K. Aika and T. Onishi, *J. Catal.*, 1988, **111**, 67-76.

[19] Y. I. Kim, S. Salim, M. J. Huq and T. E. Mallouk, *J. Am. Chem. Soc.*, 1991, **113**, 9561-9563.

[20] Y. I. Kim, S. J. Atherton, E. S. Brigham and T. E. Mallouk, *J. Phys. Chem.*, 1993, **97**, 11802-11810.

[21] G. B. Saupe, T. E. Mallouk, W. Kim and R. H. Schmehl, *J. Phys. Chem. B*, 1997, **101**, 2508-2513.

[22] R. Abe, K. Shinmei, N. Koumaura, K. Hara and B. Ohtani, *J. Am. Chem. Soc.*, 2013, **135**, 16872-16884.

[23] T. Oshima, S. Nishioka, Y. Kikuchi, S. Hirai, K. Yanagisawa, M. Eguchi, Y. Miseki, T. Yokoi, T. Yui, K. Kimoto, K. Sayama, O. Ishitani, T. E. Mallouk and K. Maeda, *J. Am. Chem. Soc.*, 2020, **142**, 8412-8420.

[24] K. Maeda and T. E. Mallouk, *Bull. Chem. Soc. Jpn.*, 2019, **92**, 38-54.

[25] I. M. Tsvetkov, E. R. Buyonova, S. V. Lymar and V. N. Parmon, *React. Kinet. Catal. Lett.*, 1983, **22**, 159-163.

[26] G. Steinberg-Yfrach, P. A. Liddell, S. C Hung, A. L. Moore, D. Gust and T. A. Moore, *Nature*, 1997, **385**, 239-241.

[27] G. Steinberg-Yfrach, J. L. Rigaud, E. N. Durantini, A. L. Moore, D. Gust and T. A. Moore, *Nature*, 1998, **392**, 479-482.

[28] H. Hu, Z. Wang, L. Cao, L. Zeng, C. Zhang, W. Lin and C. Wang, *Nat. Chem.*, 2021, **13**, 358-366.

[29] Y. H. Hong, Y. M. Lee, W. Nam and S. Fukuzumi, *J. Am. Chem. Soc.*, 2022, **144**, 695-700.

[30] R. Itagaki, S. Takizawa, H. C. Chang and A. Nakada, *Dalton Trans.*, 2022, **51**, 9467-9476.

[31] K. S. Novoselov, A. K. Geim, S. V. Morozov, D. Jiang, M. I. Katsnelson, I. V. Grigorieva, S. V. Dubonos and A. A. Firsov, *Nature*, 2005, **438**, 197-200.

[32] A. K. Geim, *Science*, 2009, **324**, 1530-1534.

[33] S. Hu, M. Lozada-Hidalgo, F. C. Wang, A. Mishchenko, F. Schedin, R. R. Nair, E. W. Hill, D. W. Boukhvalov, M. I. Katsnelson, R. A. W. Dryfe, I. V. Grigorieva, H. A. Wu and A. K. Geim, *Nature*, 2014, **516**, 227-230.

[34] C. J. Bullock and C. Bussy, *Adv. Mater. Interfaces*, 2019, **6**, 1900229.

[35] J. S. Bunch, S. S. Verbridge, J. S. Alden, A. M. van der Zande, J. M. Parpia, H. G. Craighead and P. L. McEuen, *Nano Lett.*, 2008, **8**, 2458-2462.

[36] A. K. Geim and K. S. Novoselov, *Nat. Mater.*, 2007, **6**, 183-191.

[37] L. Mogg, S. Zhang, G. P. Hao, K. Gopinadhan, D. Barry, B. L. Liu, H. M. Cheng, A. K. Geim and M. Lozada Hidalgo, *Nat. Commun.*, 2019, **10**, 4243.

[38] M. Lozada Hidalgo, S. Hu, O. Marshall, A. Mishchenko and A. N. Grigorenko, *Science*, 2016, **351**, 68-70.

[39] M. Lozada Hidalgo, S. Zhang, S. Hu, V. G. Kravets, F. J. Rodriguez, A. Berdyugin, A. Grigorenko and A. K. Geim, *Nat. Nanotech.*, 2018, **13**, 300-303.

[40] M. I. Walker, P. Braeuinger Weimer, R. S. Weatherup, S. Hofmann and U. F. Keyser, *Appl. Phys. Lett.*, 2015, **107**, 213104.

[41] A. Iwase, Y. H. Ng, Y. Ishiguro, A. Kudo and R. Amal, *J. Am. Chem. Soc.*, 2011, **133**, 11054-11057.

[42] P. Zhou, J. Yu and M. Jaroniec, *Adv. Mater.*, 2014, **26**, 4920-4935.

[43] Y. Wang, F. Wang and J. He, *Nanoscale*, 2013, **5**, 11291-11297.

[44] A. Iwase, S. Yoshino, T. Takayama, Y. H. Ng, R. Amal and A. Kudo, *J. Am. Chem. Soc.*, 2016, **138**, 10260-10264.

[45] P. Li, Y. Zhou, H. Li, Q. Xu, X. Meng, X. Wang, M. Xiao and Z. Zou, *Chem. Commun.*, 2015, **51**, 800-803.

[46] H. Li, Y. Zhou, W. Tu, J. Ye and Z. Zou, *Adv. Funct. Mater.,* 2015, **25**, 998-1013.

[47] H. Li, W. Tu, Y. Zhou and Z. Zou, *Adv. Sci.,* 2016, **3**, 1500389.

[48] J. Low, J. Yu, M. Jaroniec, S. Wageh and A. A. Al-Ghamdi, *Adv. Mater.,* 2017, **29**, 1601694.

[49] X. Wang, L. Yin and G. Liu, *Chem. Commun.,* 2014, **50**, 3460-3463.

[50] C. Liu, J. Tang, H. M. Cheng, B. Liu and P. Yang, *Nano Lett.,* 2013, **13**, 2989-2992.

[51] Y. H. Ng, A. Iwase, A. Kudo and R. Amal, *J. Phys. Chem. Lett.,* 2010, **1**, 2607-2612.

[52] H. Zhang, X. Lv, Y. Li, Y. Wang and J. Li, *ACS Nano,* 2010, **4**, 380-386.

[53] W. Tu, Y. Zhou, Q. Liu, S. Yan, S. Bao, X. Wang, M. Xiao and Z. Zou, *Adv. Funct. Mater.,* 2013, **23**, 1743-1749.

[54] W. Tu, Y. Zhou and Z. Zou, *Adv. Funct. Mater.,* 2013, **23**, 4996-5008.

[55] K. P. Loh, Q. L. Bao, P. K. Ang and J. X. Yang, *J. Mater. Chem.,* 2010, **20**, 2277- 2289.

[56] R. Czerw, B. Foley, D. Tekleab, A. Rubio, P. M. Ajayan and D. L. Carroll, *Phys. Rev. B,* 2002, **66**, 033408.

[57] V. Georgakilas, M. Otyepka, A. B. Bourlinos, V. Chandra, N. Kim, K. C. Kemp, P. Hobza, R. Zboril and K. S. Kim, *Chem. Rev.,* 2012, **112**, 6156-6214.

[58] S. P. Surwade, S. N. Smirnov, I. V. Vlassiouk, R. R. Unocic, G. M. Veith, S. Dai and S. M. Mahurin, *Nat. Nanotechnol.,* 2015, **10**, 459-464.

[59] W. J. Jo, G. Katsoukis and H. Frei. *Adv. Funct. Mater.,* 2020, **30**, 1909262.

[60] H. Zhang, I. Weiss, I. Rudra, W. J. Jo, S. Kellner, G. Katsoukis, E. Galoppini and H. Frei. *ACS Appl. Mater. Interfaces,* 2021, **13**, 23532-23546.

[61] W. J. Jo, H. Zhang, G. Katsoukis and H. Frei, in *Ultrathin Oxide Layers for Solar and Electrocatalytic Systems*, ed. H. Frei and D. V. Esposito, The Royal Society of Chemistry, London, Energy Environ. Ser. 30, 2022, Ch. 11, 298-341.

[62] G. Katsoukis and H. Frei, *ACS Appl. Mater. Interfaces*, 2018, **10**, 31422-31432.

[63] H. S. Soo, A. Agiral, A. Bachmeier and H. Frei, *J. Am. Chem. Soc.*, 2012, **134**, 17104-17116.

[64] A. Agiral, H. S. Soo and H. Frei, *Chem. Mater.*, 2013, **25**, 2264-2273.

[65] J. A. Cornejo, H. Sheng, E. Edri, C. A. Ajo-Franklin and H. Frei, *Nat. Commun.*, 2018, **9**, 2263.

[66] G. Katsoukis, W. J. Jo and H. Frei, *J. Phys. Chem. C*, 2019, **123**, 18905-18913.

[67] E. Edri and H. Frei, *J. Phys. Chem. C*, 2015, **119**, 28326-28334.

[68] G. Katsoukis and H. Frei, *J. Chem. Phys.*, 2019, **150**, 041501.

[69] E. Edri, J. K. Cooper, I. D. Sharp, D. M. Guldi and H. Frei, *J. Am. Chem. Soc.*, 2017, **139**, 5458-5466.

[70] R. A. Marcus and N. Sutin, *Biochim. Biophys. Acta*, 1985, **811**, 265-322.

[71] K. Sun, I. A. Moreno Hernandez, W. C. Schmidt, X. Zhou, J. C. Crompton, R. Liu, F. H. Saadi, Y. Chen, K. M. Papadantonakis and N. S. Lewis, *Energy Environ. Sci.*, 2017, **10**, 87-1002.

[72] N. Y. Labrador, E. L. Songcuan, C. DeSilva, H. Chen, S. J. Kurdziel, R. K. Ramachandran, C. Detavernier and D. V. Esposito, *ACS Catal.*, 2018, **8**, 1767-1778.

[73] Solar Spectra, National Renewable Energy Laboratory, Golden, CO, USA, http://rredc.nrel.gov/solar/spectra/am1.5 (accessed February 2023).

[74] C. J. T. de Grotthuss, *Ann. Chim.*, 1806, **25**, 54-74.

[75] G. Lockwood and S. H. Carofalini, *J. Chem. Phys.*, 2009, **131**, 074703.

[76] J. C. Fogarty, H. M. Aktulga, A. Y. Grama, A. C. T. van Duin and S. A. Pandit, *J. Chem. Phys.*, 2010, **132**, 174704.

[77] H. A. Kurtz and S. P. Karna, *IEEE Trans. Nucl. Sci.*, 1999, **46**, 1574-1579.

[78] M. L. Macnaughtan, H. S. Soo and H. Frei, *J. Phys. Chem. C*, 2014, **118**, 7874-7885.

[79] W. Kim, G. Yuan, B. A. McClure and H. Frei, *J. Am. Chem. Soc.*, 2014, **136**, 11034-11042.

[80] A. D. Hill, G. Katsoukis and H. Frei, *J. Phys. Chem. C*, 2018, **122**, 20176-20185.

[81] W. Kim, E. Edri and H. Frei, *Acc. Chem. Res.*, 2016, **49**, 1634-1645.

[82] W. Kim, B. A. McClure, E. Edri and H. Frei, *Chem. Soc. Rev.*, 2016, **45**, 3221-3243.

[83] E. Edri, S. Aloni and H. Frei, *ACS Nano*, 2018, **12**, 533-541.

[84] A. J. Clough, J. W. Yoo, M. H. Mecklenburg and S. C. Marinescu, *J. Am. Chem. Soc.*, 2015, **137**, 118-121.

[85] L. S. Xie, G. Skorupskii and M. Dinca, *Chem. Rev.*, 2020, **120**, 8536-8580.

[86] E. M.Johnson, S. Ilic and A. J. Morris, *ACS Cent. Sci.*, 2021, **7**, 445-453.

[87] H. Furukawa, K. E. Cordova, M. O'Keeffe and O. M. Yaghi, *Science*, 2013, **341**, 1230444.

[88] E. Virmani, J. M. Rotter, A. Maehringer, T. von Zons, A. Godt, T. Bein, S. Wuttke and D. D. Medina, *J. Am. Chem. Soc.*, 2018, **140**, 4812-4819.

[89] K. Sumida, D. L. Rogow, J. A. Mason, T. M. McDonald, E. D. Bloch, Z. R. Herm, T. H. Bae and J. R. Long, *Chem. Rev.*, 2012, **112**, 724-781.

[90] M. P. Suh, H. J. Park, T. K. Prasad and D. W. Lim, *Chem. Rev.*, 2012, **112**, 782-835.

[91] J. A. Mason, M. Veenstra and J. R. Long, *Chem. Sci.*, 2014, **5**, 32-51.

[92] K. Adil, Y. Belmabkhout, R. S. Pillai, A. Cadiau, P. M. Bhatt, A. H. Assen, G. Maurin and M. Eddaoudi, *Chem. Soc. Rev.,* 2017, **46**, 3402-3430.

[93] S. Zhang, L. Shen, H. Deng, Q. Liu, X. You, J. Yuan, Z. Jiang and S. Zhang, *Adv. Mater.,* 2022, **34**, 2108457.

[94] S. Takaishi, M. Hosoda, T. Kajiwara, H. Miyasaka, M. Yamashita, Y. Nakanishi, Y. Kitagawa, K. Yamaguchi, A. Kobayashi and H. Kitagawa, *Inorg. Chem.*, 2009, **48**, 9048-9050.

[95] M. L. Aubrey, B. M. Wiers, S. C. Andrews, T. Sakurai, S. E. Reyes-Lillo, S. M. Hamed, C. J. Yu, L. E. Darago, J. A. Mason, J. O. Baeg, F. Grandjean, G. J. Long, S. Seki, J. B. Neaton, P. Yang and J. R. Long, *Nat. Mater.,* 2018, **17**, 625-632.

[96] L. S. Xie, L. Sun, R. Wan, S. S. Park, J. A. DeGayner, C. H. Hendon and M. Dinca, *J. Am. Chem. Soc.,* 2018, **140**, 7411-7414.

[97] F. Gandara, F. J. Uribe-Romo, D. K. Britt, H. Furukawa, L. Lei, R. Cheng, X. Duan, M. O'Keefe and O. M. Yaghi, *Chem. Eur. J.*, 2012, **18**, 10595-10601.

[98] J. G. Park, M. L. Aubrey, J. Oktawiec, K. Chakarawet, L. E. Darago, F. Grandjean, G. J. Long and J. R. Long, *J. Am. Chem. Soc.*, 2018, **140**, 8526-8534.

[99] T. C. Narayan, T. Miyakai, S. Seki and M. Dinca, *J. Am. Chem. Soc.,* 2012, **134**, 12932-12935.

[100] S. S. Park, E. R. Hontz, L. Sun, C. H. Hendon, A. Walsh, T. Van Voorhis and M. Dinca, *J. Am. Chem. Soc.*, 2015, **137**, 1774-1777.

[101] R. W. Day, D. K. Bediako, M. Rezaee, L. R. Parent, G. Skorupskii, M. Q. Arguilla, C. H. Hendon, I. Stassen, N. Gianneschi, P. Kim and M. Dinca, *ACS Cent. Sci.,* 2019, **5**, 1959-1964.

[102] E. M. Miner, T. Fukushima, D. Sheberla, L. Sun, Y. Surendranath and M. Dinca, *Nat. Commun.,* 2016, **7**, 10942.

[103] M. A. Solomos, F. J. Claire and T. J. Kempa, *J. Mater. Chem. A,* 2019, **7**, 23537-23562.

[104] M. Ko, L. Mendecki and K. A. Mirica, *Chem. Commun.*, 2018, **54**, 7873-7891.

[105] W. Zheng, C. S. Tsang, L. Y. S. Lee and K. Y. Wong, *Mater. Today Chem.*, 2019, **12**, 34-60.

[106] Y. Ye, L. Gong, S. Xiang, Z. Zhang and B. Chen, *Adv. Mater.,* 2020, **32**, 1907090.

[107] N. T. T. Nguyen, H. Furukawa, F. Gandara, C. A. Trickett, H. M. Jeong, K. E. Cordova and O. M. Yaghi, *J. Am. Chem. Soc.*, 2015, **137**, 15394-15397.

[108] M. Sadakiyo, T. Yamada and H. Kitagawa, *J. Am. Chem. Soc.*, 2009, **131**, 9906-9907.

[109] R. Dong, M. Pfeffermann, H. Liang, Z. Zheng, X. Zhu, J. Zhang and X. Feng, *Angew. Chem. Int. Ed.*, 2015, **54**, 12058-12063.

[110] R. Dong, Z. Zheng, D. C. Tranca, J. Zhang, N. Chandrasekhar, S. Liu, X. Zhuang, G. Seifert and X. Feng, *Chem. Eur. J.*, 2017, **23**, 2255-2260.

[111] C. A. Downes, A. J. Clough, K. Chen, J. W. Yoo and S.C. Marinescu, *ACS Appl. Mater. Interfaces,* 2018, **10**, 1719-1727.

[112] S. Zhao, Y. Wang, J. Dong, C. T. He, H. Yin, P. An, K. Zhao, X. Zhang, C. Gao, L. Zhang, J. Lv, J. Wang, J. Zhang, A. M. Khattak, N. A. Khan, Z. Wei, J. Zhang, S. Liu, H. Zhao and Z. Tang, *Nat. Energy*, 2016, **1**, 16184.

[113] J. Duan, S. Chen and C. Zhao, *Nat. Commun.*, 2017, **8**, 15341.

[114] S. Navalon, A. Dhakshinamoorthy, M. Alvaro, B. Ferrer and H. Garcia, *Chem. Rev.*, 2023, **123**, 445-490.

[115] S. Lin, Y. Pineda Galvan, W. A. Maza, C. C. Epley, J. Zhu, M. C. Kessinger, Y. Pushkar and A. J. Morris, *ChemSusChem,* 2017, **10**, 514-522.

[116] H. Wu, J. Wang, W. Jin and Z. Wu, *Nanoscale*, 2020, **12**, 18497-18522.

[117] N. Kornienko, Y. Zhao, C. K. Kley, D. Kim, S. Lin, C. J. Chang, O. M. Yaghi and P. Yang, *J. Am. Chem. Soc.,* 2015, **137**, 14129-14135.

[118] S. Lin, C. S. Diercks, Y. B. Zhang, N. Kornienko, E. M. Nichols, Y. Zhao, A. R. Paris, D. Kim, P. Yang, O. M. Yaghi and C. J. Chang, *Science*, 2015, **349**, 1208-1213.

[119] I. Hod, M. D. Sampson, P. Deria, C. P. Kubiak, O. K. Fahra and J. T. Hupp, *ACS Catal.,* 2015, **5**, 6302-6309.

[120] R. Matheu, E. Gutierrez-Puebla, M. A. Monge, C. S. Diercks, J. Kang, M. S. Prevot, X. Pei, N. Hanikel, B. Zhang, P. Yang and O. M. Yaghi, *J. Am. Chem. Soc.*, 2019, **141,** 17081-17085.

[121] J. Y. Xue, C. Li, F. L. Li, H. W. Gu, P. Braustein and J. P. Lang, *Nanoscale*, 2020, **12**, 4816-4825.

[122] P. Thangasamy, S. Shanmuganathan and V. Subramanian, *Nanoscale Adv.*, 2020, **2**, 2073-2079.

[123] Z. M. Wang, W. Peng, Y. Takenaka, N. Yoshizawa, K. Kosuge, W. Wang and G. A. Ozin, *Adv. Funct. Mater.,* 2017, **27**, 1704066.

[124] K. Jayaramulu, S. Mukherjee, D. M. Morales, D. P. Dubal, A. K. Nanjundan, , A. Schneemann, J. Masa, S. Kment, W. Schuhmann, M. Otyepka, R. Zboril and R. A. Fischer, *Chem. Rev.,* 2022, **122**, 17241-17338.

[125] K. Wang, K. N. Hui, K. S. Hui, S. Peng and Y Xu, *Chem. Sci.,* 2021, **12**, 5737-5766.

[126] Y. Zheng, S. Zheng, H. Xue and H. Pang, *Adv. Funct. Mater.*, 2018, **28**, 1804950.

[127] J. Multia and M. Karppinen, *Adv. Mater. Interfaces*, 2022, **9**, 2200210.

[128] F. Niu, D. Wang, F. Li, Y. Liu, S. Shen and T. J. Meyer, *Adv. Energy Mater.*, 2020, **10**, 1900399.

[129] T. T. Li, B. Shan and T. J. Meyer, *ACS Energy Lett.*, 2019, **4**, 629-636.

[130] R. J. Kamire, M. B. Majewski, W. L. Hoffeditz, B. T. Phelan, O. K. Farha, J. T. Hupp and M. R. Wasielewski, *Chem. Sci.*, 2017, **8**, 541-549.

[131] S. Zhang, L. Shen, H. Deng, Q. Liu, X. You, J. Yuan, Z. Jiang and S. Zhang, *Adv. Mater.*, 2022, **34**, 2108457.

[132] D. Perego, S. Franz, M. Bestetti, L. Cattaneo, S. Brivio, G. Tallarida and S. Spiga, *Nanotechnology*, 2013, **24**, 045302.

[133] L. Wen, R. Xu, Y. Mi and Y. Lei, *Nat. Nanotechnol.*, 2017, **12**, 244-250.

[134] H. A. Park, S. Liu, Y. Oh, P. A. Salvador, G. S. Rohrer and M. F. Islam, *ACS. Nano*, 2017, **11**, 2150-2159.

[135] A. J. Marden, M. C. Asensio, J. Avila, P. Dudin, A. Barinov, P. Moras, P. M. Shewerdyaeva, T. W. White, I. Maskery, G. Costantini, N. R. Wilson and G. R. Bell, *Phys. Status Solidi RRL*, 2013, **7**, 643-646.

[136] Y. Tchoe. J. Jo, H. S. Kim, H. Kim, H. Baek, K. Lee, D. Yoo, W. J. Choi, M. Kim and G. C.Yi, *NPG Asia Materials*, 2021, **13**, 33.

[137] M. S. Sander, M. J. Cote, W. Gu, B. M. Kile and C. P. Tripp, *Adv. Mater*, 2004, **16**, 2052-2057.

[138] A. Ruiz Clavijo, O. Caballero Calero and M. Martin-Gonzalez, *Nanoscale*, 2021, **13**, 2227-2265.

[139] S. J. Ku, G. C. Jo, C. H. Bak, S. M. Kim, Y. R. Shin, K. H. Kim, S. H. Kwon and J. B. Kim, *Nanotechnology*, 2013, **24**, 085301.

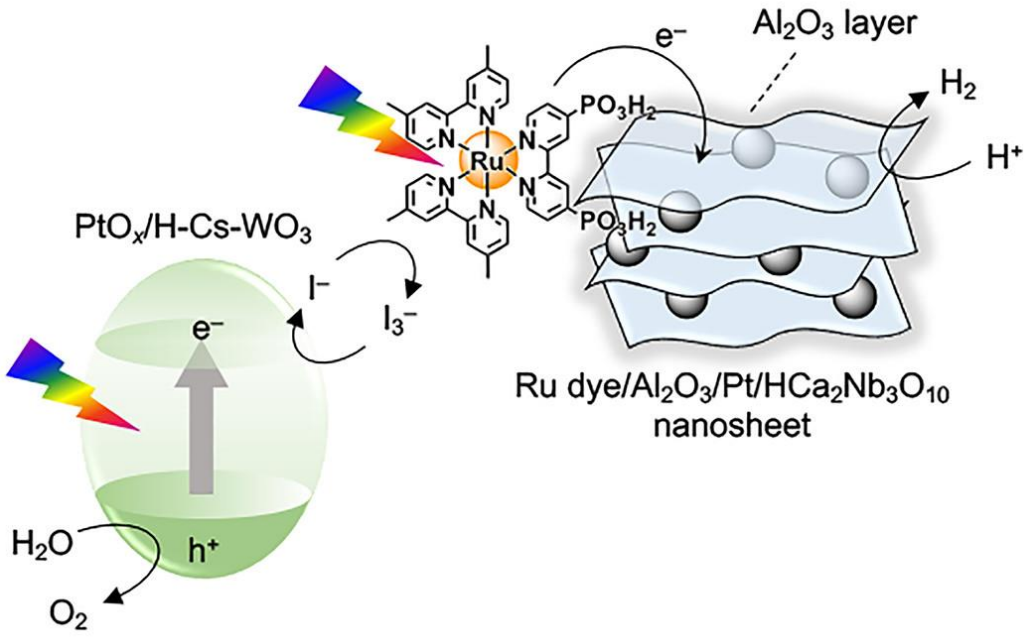

Figure 1: Z-scheme tandem system for visible light driven overall water splitting using Al_2O_3 modified niobate nanosheets with Pt nanoparticle catalyst for H^+ reduction compartmentalized in interlayer spaces and I^-/I_3^- as electron transfer shuttle. Efficiency enhancement is achieved by blocking access of I_3^- to Pt by electrostatic repulsion of the negatively charged niobate sheets. Reproduced from ref. 23 with permission from the American Chemical Society, Copyright 2020.

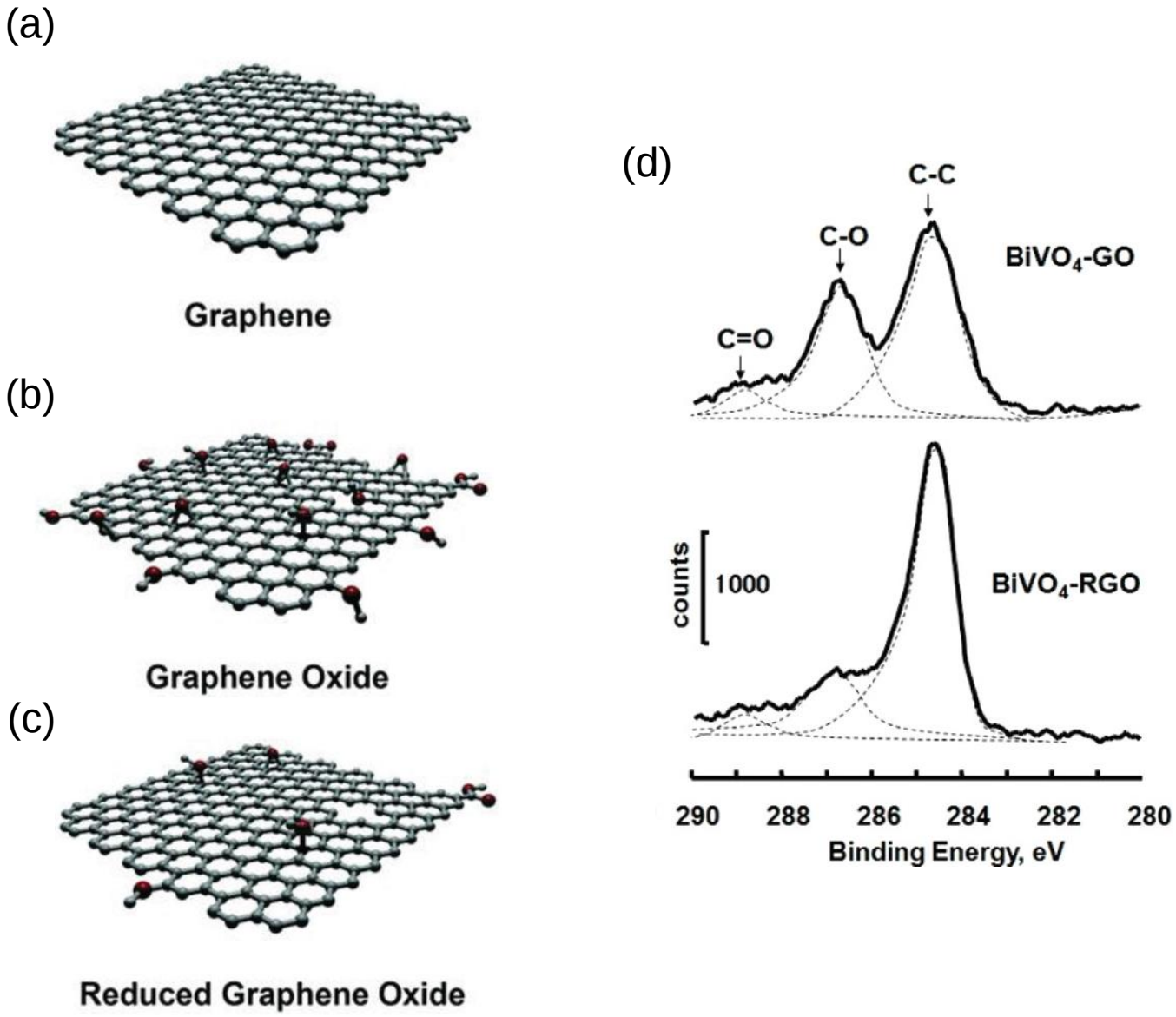

Figure 2: Graphene. **(a)** Defect-free single graphene layer. **(b)** Graphene oxide. **(c)** Reduced graphene oxide (RGO). Reproduced from ref. 34 with permission from John Wiley & Sons, Copyright 2019. WILEY-VCH Verlag GmbH & Co. KGaA, Weinheim. **(d)** Carbon (1s) XPS of graphene oxide before (top) and after reduction by visible light excitation of $BiVO_4$ photocathode for 3 h (bottom). The C-O (epoxy and hydroxyl, 286.6 eV) and carboxylate C=O (288.9 eV) show a sharp decrease while the C-C signal (284.5 eV) increases. Reproduced from ref. 51 with permission from the American Chemical Society, Copyright 2018.

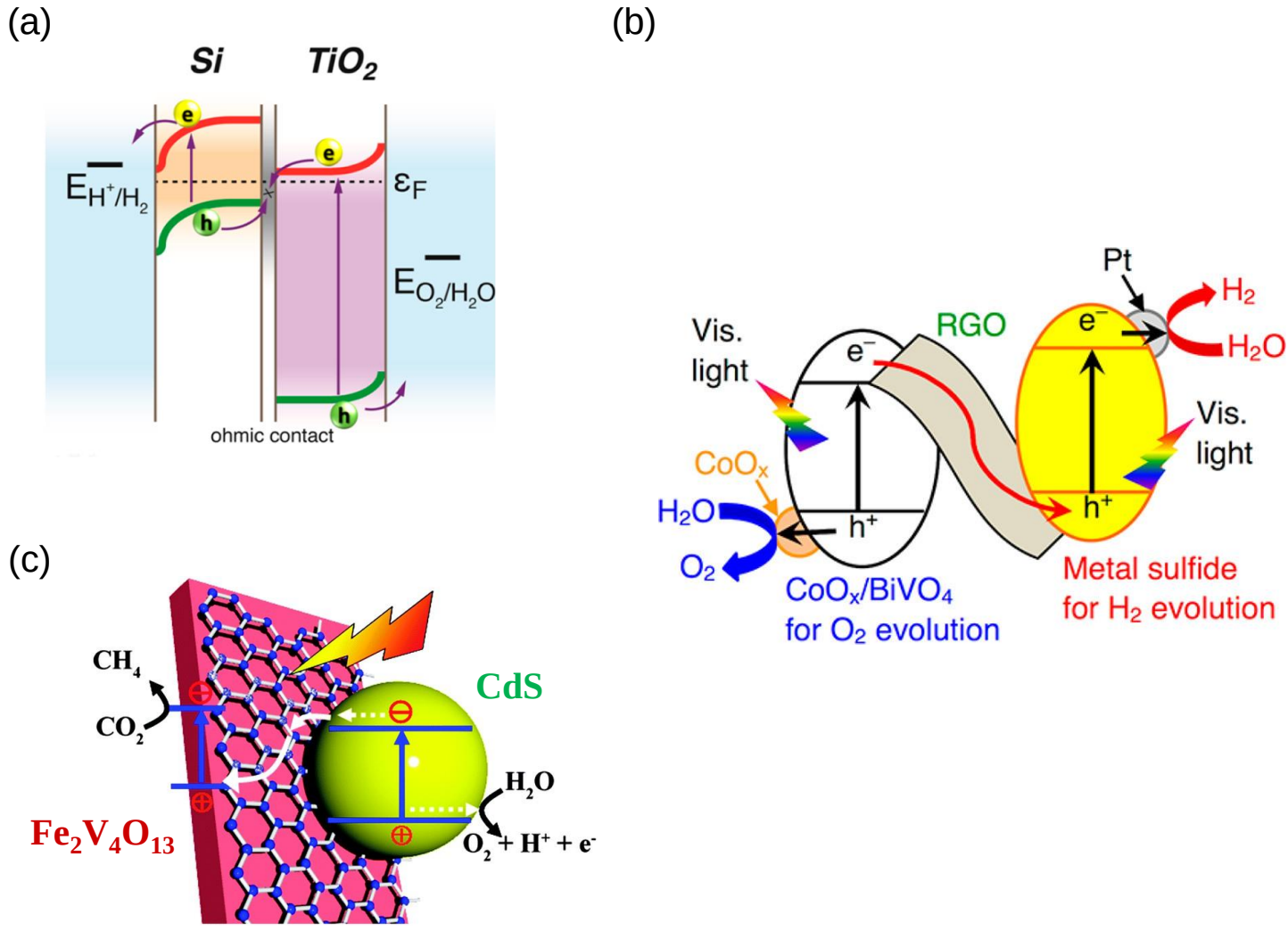

Figure 3: Graphene serving as ohmic contact of Z-scheme tandem photosystems. **(a)** Ohmic contact enabling charge flow of TiO_2-Si Z-scheme heterostructure for photocatalytic H_2O splitting. The photogenerated electrons in Si and holes in TiO_2 move to aqueous interface to perform water splitting, while the holes in Si and electrons in TiO_2 recombine at the ohmic contact between the two semiconductors. Reproduced from ref. 50 with permission from the American Chemical Society, Copyright 2013. **(b)** Photosystem for H_2O splitting with graphene contact between $BiVO_4$-CoO_x oxidation and CuGaS -Pt reduction photocatalysts. Reproduced from ref. 44 with permission from the American Chemical Society, Copyright 2016. **(c)** Photosystem for CO_2 reduction by H_2O with graphene contact between CdS oxidation and $Fe_2V_4O_{13}$ reduction photocatalyts. Reproduced from ref. 45 with permission from the Royal Society of Chemistry.

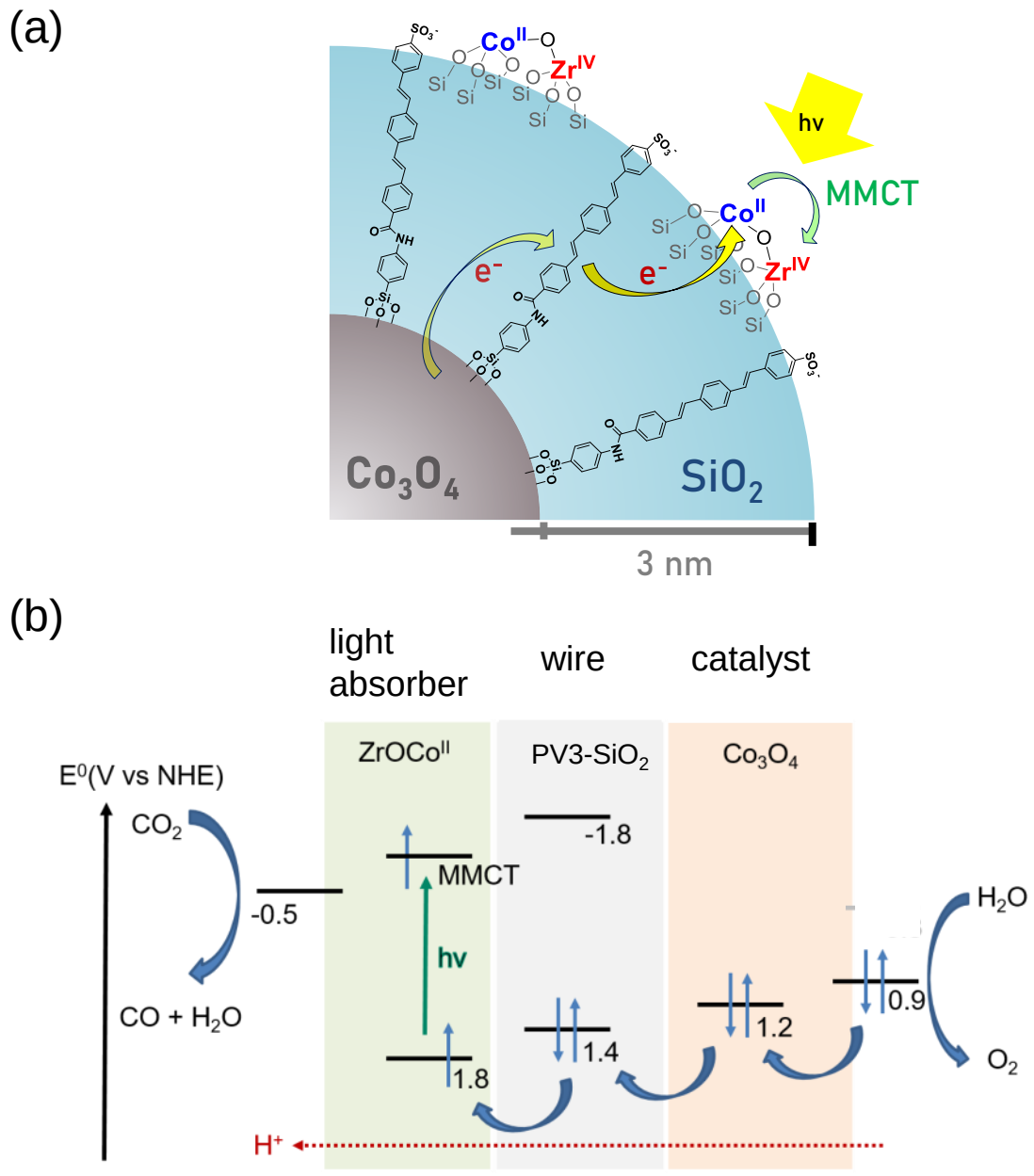

Figure 4: Ultrathin amorphous silica membrane with embedded molecular wires. **(a)** Schematic of visible light driven hole transfer from transient Co^{III} formed by $Zr^{IV}OCo^{II} \rightarrow Zr^{III}OCo^{III}$ charge transfer photoexcitation via embedded molecular wire to Co_3O_4 catalyst. Reproduced from ref. 62 with permission from the American Chemical Society, Copyright 2018. **(b)** Energy level alignment of light absorber, PV3 wire, and catalyst for light-induced directional charge transfer for driving H_2O oxidation and CO_2 reduction. Oxidation and reduction catalysis occurs at the gas/solid interface, with an H^+ gradient developing across the nanomembrane during photocatalytic H_2O oxidation. The SiO_2 membrane blocks crossover of reactants and products, except for H^+. Adapted from ref. 82 with permission from the Royal Society of Chemistry.

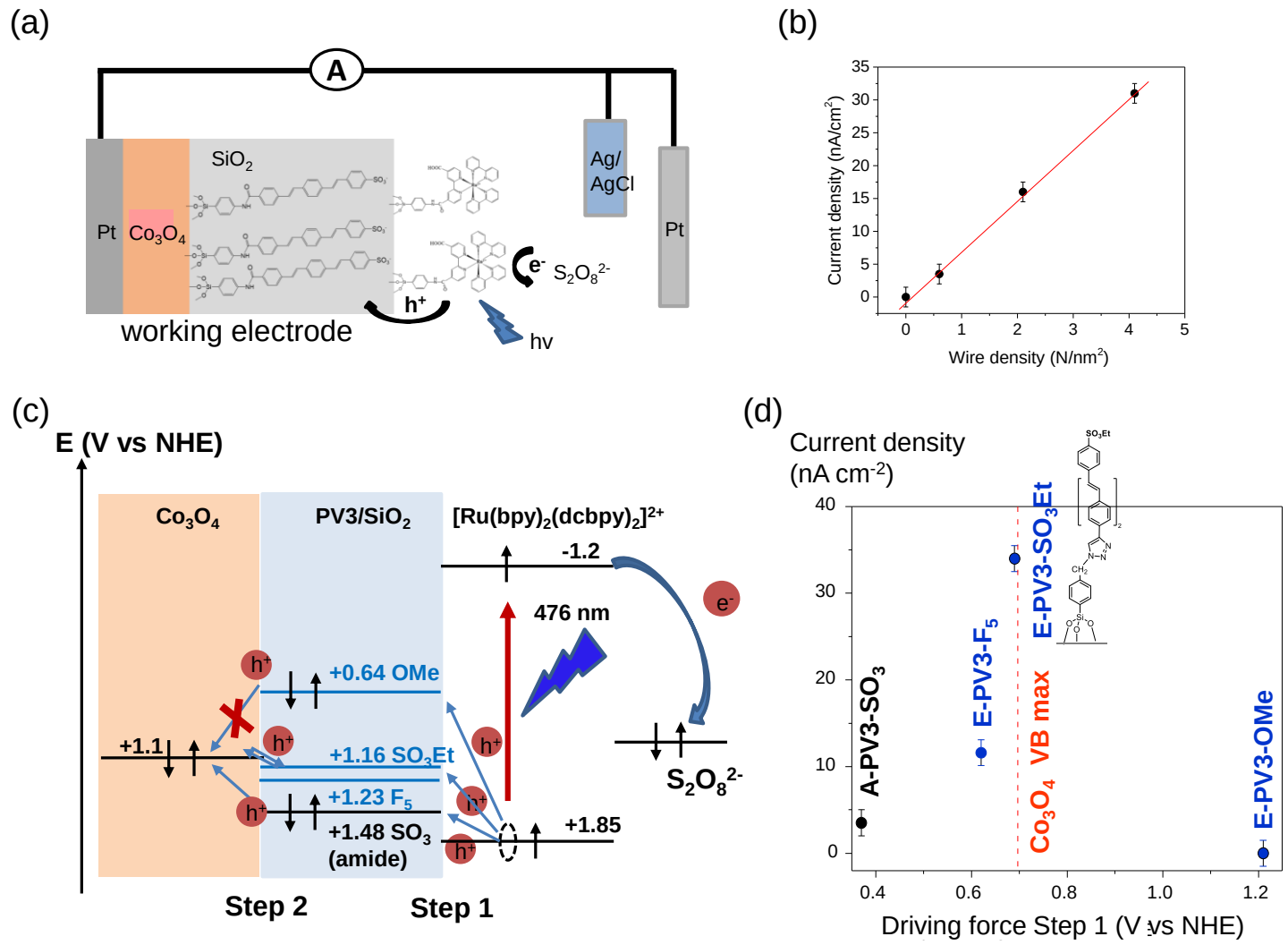

Figure 5: Short circuit photocurrent measurements for assessing electron conductivity. **(a)** Schematic of three-electrode cell with working Pt electrode onto which 12 nm Co_3O_4 followed by 3 nm silica membrane with embedded TMS-Am-PV3-SO_3 wires are deposited. Covalently anchored $[Ru(bpy)_2(dcbpy)]^{2+}$ light absorbers are also shown. **(b)** Wire density dependence of photocurrent. **(c)** Energy level alignment of the HOMO of molecular wires with the HOMO of Ru light absorber and Co_3O_4 catalyst valence band. Anchored wires are abbreviated OMe for E-PV3-OMe, SO_3Et for E-PV3-SO_3Et, F_5 for E-PV3-F_5, and SO_3 for A-PV3-SO_3. The corresponding molecular structures are shown in Figure 5. **(d)** Photocurrent dependence on the HOMO potential of the embedded wire molecule, normalized for wire density of 0.6 nm^{-2}. Reproduced from ref. 60 with permission from the American Chemical Society, Copyright 2021.

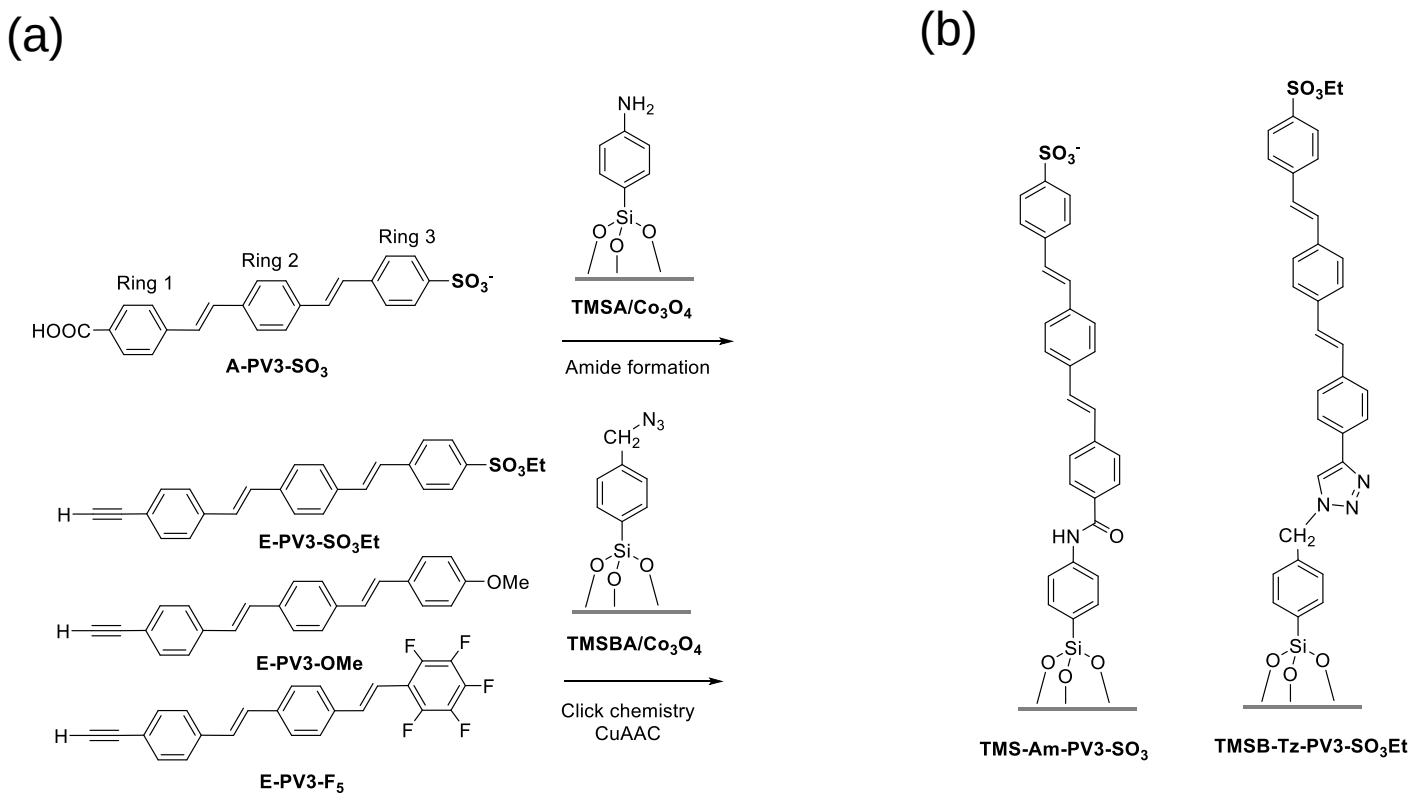

Figure 6: Functionalized wire molecules with electron-donating and -withdrawing groups. **(a)** Free wires. **(b)** Wires attached to anchor by amide or triazole linker. Corresponding HOMO potentials of wire linked to the anchor (vs. NHE) are shown in schematic Figure 4c. Reproduced from ref. 60 with permission from the American Chemical Society, Copyright 2021.

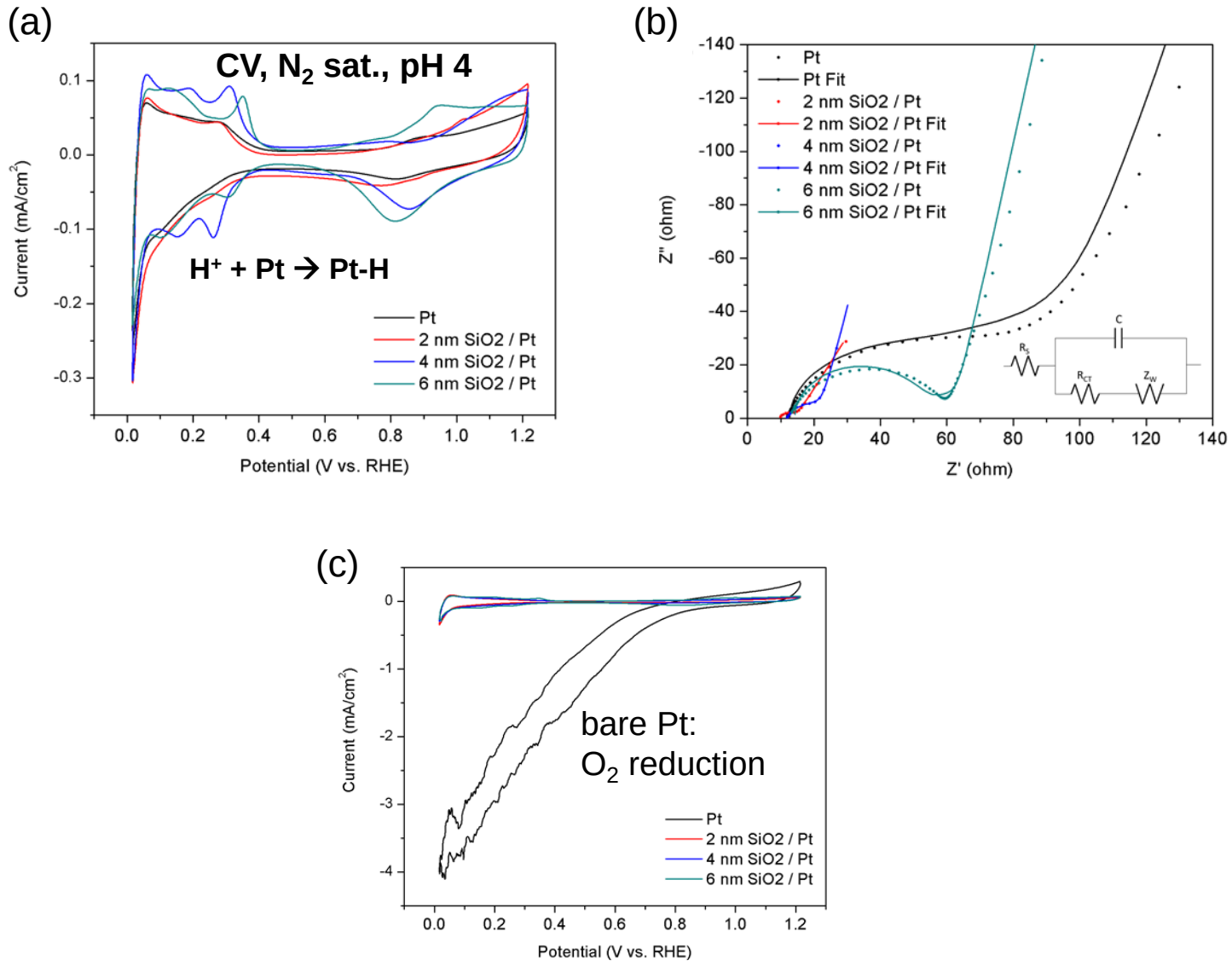

Figure 7: Proton conductivity and O_2 blocking property of ultrathin silica membrane. **(a)** Cyclic voltammogram (CV) of bare Pt electrode (black trace) and Pt covered with 2, 4, and 6 nm SiO_2 (red, blue, and green traces) at 298 K in N_2-saturated aqueous 0.5 M Na_2SO_4 solution at pH 4. **(b)** Electrochemical impedance spectra in N_2-saturated pH 4 electrolyte solution used for (a). Applied potential 0.096 V vs. RHE. The dots in the plot are the experimental data and the solid lines represent the results of fitting the data to the equivalent circuit (Randles circuit) shown in the inset. **(c)** CV in O_2-bubbled electrolyte solution under the same conditions as used for (a). Reproduced from ref. 59 with permission from John Wiley & Sons, Copyright 2019. WILEY-VCH Verlag GmbH & Co. KGaA, Weinheim.

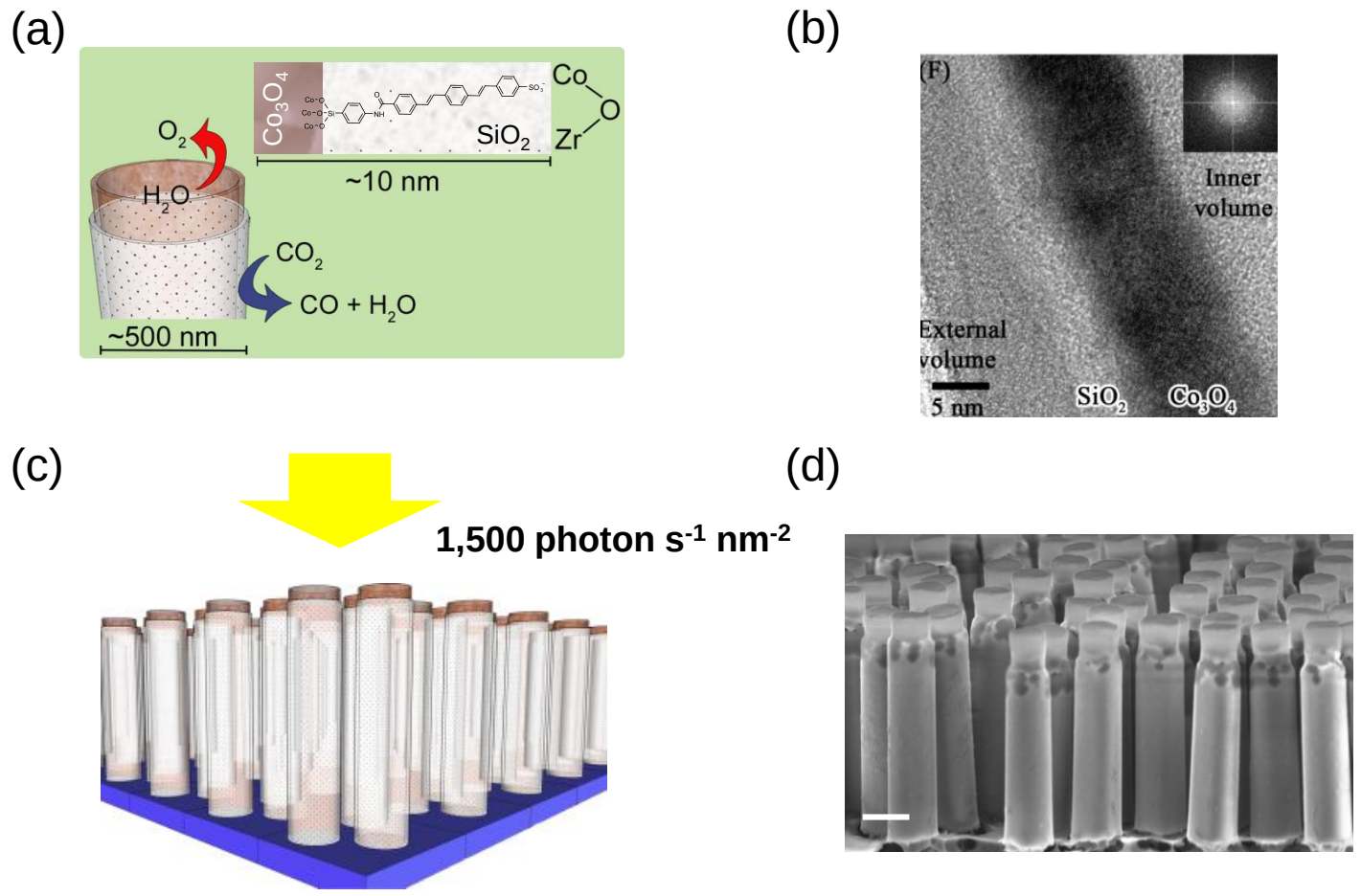

Figure 8: Co oxide-silica core-shell nanotube featuring a silica nanomembrane as complete photosynthetic unit for CO_2 photoreduction by H_2O. **(a)** Schematic of design. **(b)** HR-TEM image showing a longitudinal cross-section of a single Co_3O_4-SiO_2 core-shell nanotube wall. Inset: fast Fourier transform (FFT) image of the crystalline Co_3O_4 layer. Reproduced from ref. 83 with permission from the American Chemical Society, Copyright 2018. **(c)** Schematic of core-shell nanotube array. **(d)** SEM of section of macroscale $Co_3O_4/SiO_2/TiO_2$ nanotube array after complete removal of sacrificial Si template. Scale bar: 500 nm. Reproduced from ref. 61 with permission from the Royal Society of Chemistry.

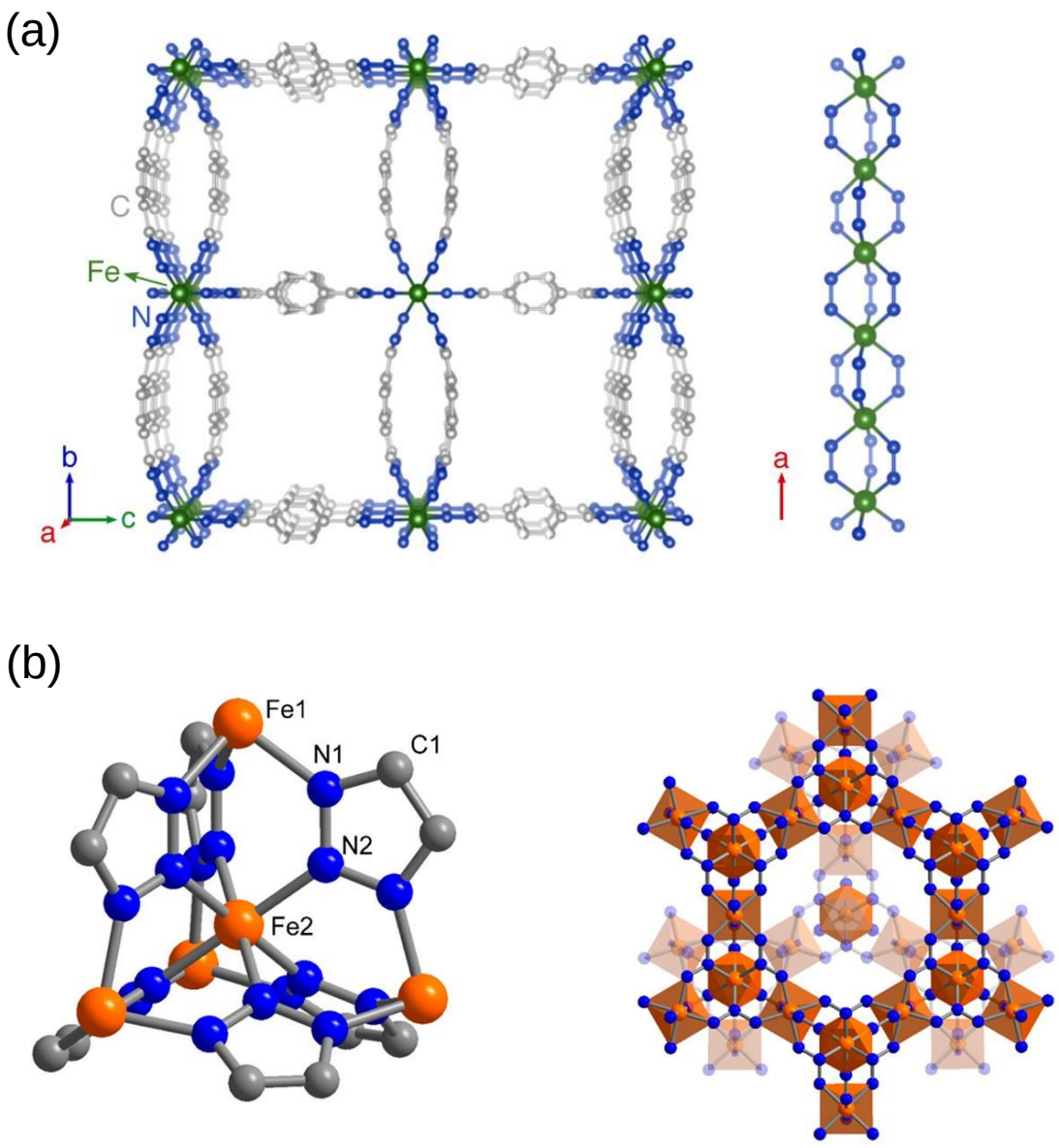

Figure 9: Highly electron conductive mixed-valence Fe azolate MOFs. **(a)** Iron tetrazolate MOF crystal structure (left) and $(Fe\text{-}N\text{-}N)_{\infty}$ chains serving as charge transport conduits (right). Fe, green dots; N, blue dots. Reproduced from ref. 96 with permission from the American Chemical Society, Copyright 2018. **(b)** Structure of secondary building unit of MOF $Fe(1,2,3\text{-triazolate})_2(BF_4)_x$ (left) and Fe-N sublattice (right). Reproduced from ref. 98 with permission from the American Chemical Society. Copyright 2018.

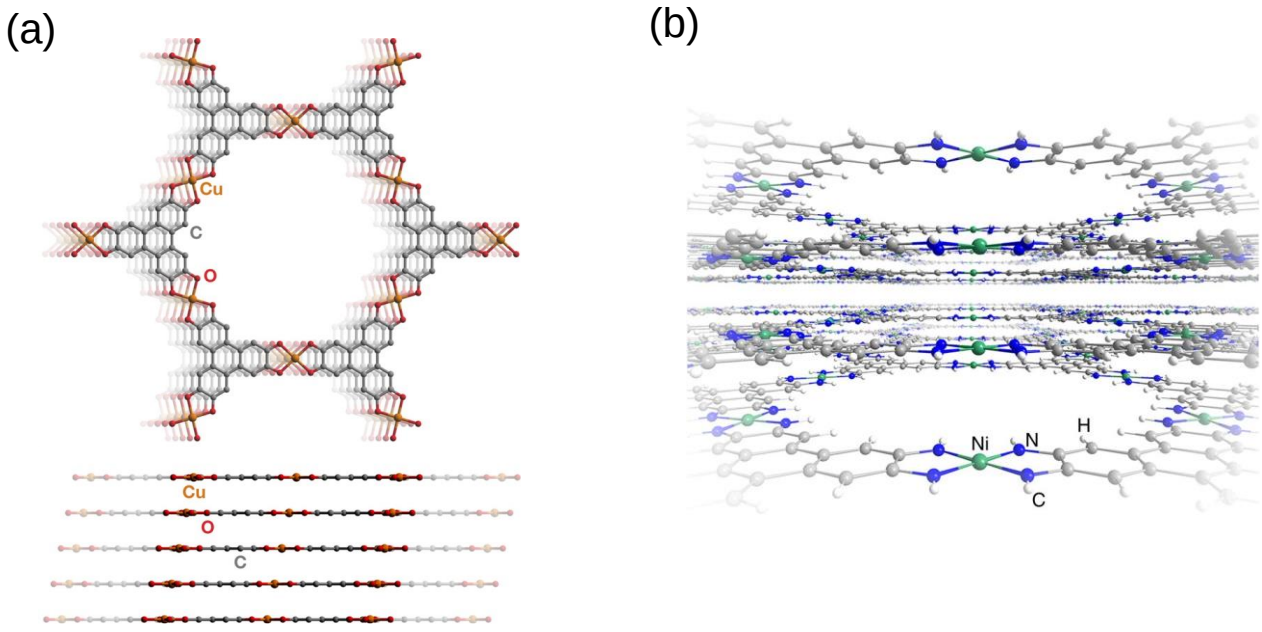

Figure 10: Highly conductive two-dimensional MOFs. **(a)** 2D honeycomb layers of $Cu_3(HOTP)_2$ with square planar Cu centers bridging triphenylene-based linkers (top). Continuous slipped stacking arrangement of $Cu_3(HOTP)_2$ layers providing π-π interaction is also shown (bottom). Reproduced from ref. 101 with permission from the American Chemical Society, Copyright 2019. **(b)** Two-dimensional layered structure of $Ni_3(HITP)_2$ MOF. Reproduced from ref. 102 with permission from Springer Nature, Copyright 2016.

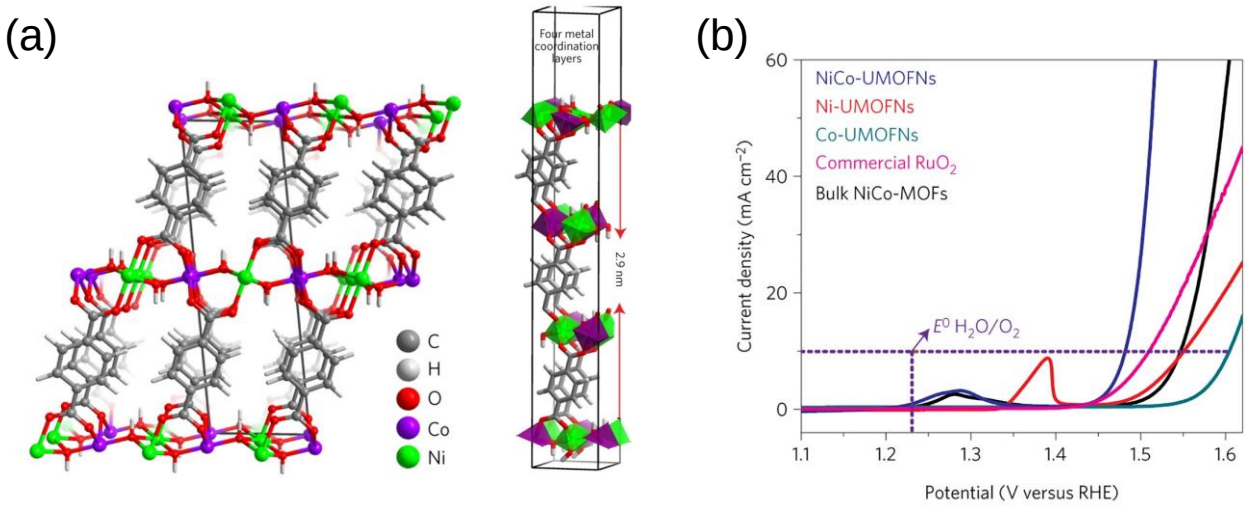

Figure 11: Ultrathin bimetallic NiCo MOF for electrocatalytic O_2 reduction. **(a)** MOF crystal structure. **(b)** Polarization curves of bimetallic NiCo MOF (dark blue trace) compared with monometallic Ni (red), Co (light blue), RuO_2 (purple) and bulk NiCo MOF (black). Reproduced from ref. 112 with permission from Springer Nature, Copyright 2016.

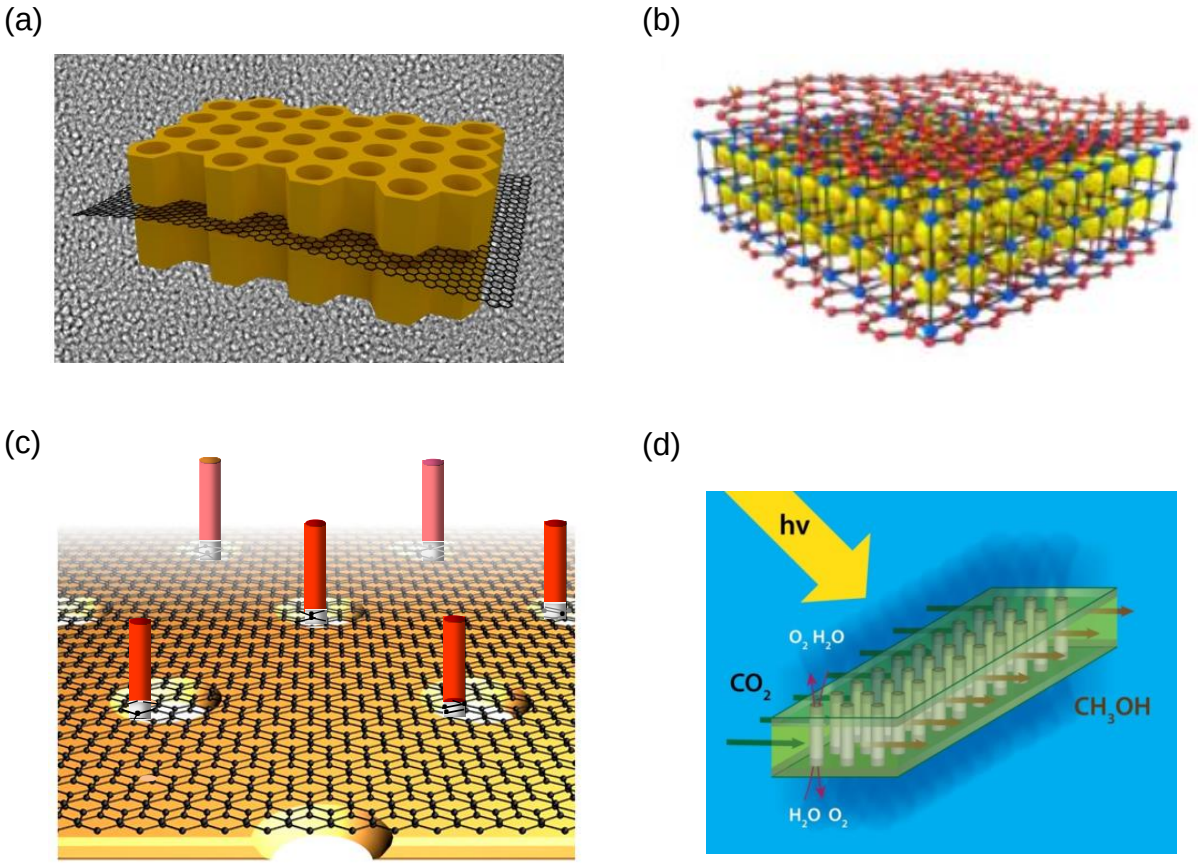

Figure 12: Proposed designs of using ultrathin conductive separation membranes for nanoscale integrated photosystems. **(a)** Schematic of graphene membrane sandwiched between nanoporous silica layers of tens of nm thickness with vertically aligned pores. Reproduced from ref. 123 with permission from John Wiley & Sons, Copyright 2017. WILEY-VCH Verlag GmbH & Co. KGaA, Weinheim. **(b)** MOF of structure $Zr_6O_4(OH)_4(bdc\text{-}NH_2)_6$, $bdc\text{-}NH_2$ = 2-amino-1,4-benzenedicarboxylate (blue/yellow) interfaced with graphene membrane (red). Reproduced from ref. 124 with permission from the American Chemical Society, Copyright 2022. **(c)** Section of array of semiconductor particle Z-scheme, here in the form of nanorods, with graphene sheet serving as ohmic contact of photoanode/cathode and as proton transmitting separation membrane. Portion of figure adapted from ref. 136 under Creative Commons licence http://creativecommons.org/licenses/by/4.0/. **(d)** Complete Co oxide - silica nanotube array with top and bottom cover for permanent separation, on all length scales, of evolving CO_2 reduction product (gallery space between the top and bottom covers) and O_2 (inside tubes and external space). Reproduced from ref. 82 with permission from the Royal Society of Chemistry.

TOC

Ultrathin separation membranes of ten nanometer thickness or less capable of separating small molecules for avoiding back reactions while providing adequate rates for electron and proton transport open up nanoscale integrated artificial photosystems